Sparser and Less Efficient Hippocampal-Prefrontal Projections account for Developmental Network Dysfunction in a Model of Psychiatric Risk Mediated by Gene-Environment Interaction

1

2

3

4 **Sparser and less efficient hippocampal-prefrontal projections**
5 **account for developmental network dysfunction in a model of**
6 **psychiatric risk mediated by gene-environment interaction**

7
8
9 Lingzhen Song[1#], Xiaxia Xu[1#], Peggy Putthoff[1], David Fleck[2], Marc Spehr[2] and
10 Ileana L. Hanganu-Opatz[1]*

11
12 [1]Institute of Developmental Neurophysiology, Center for Molecular Neurobiology, University
13 Medical Center Hamburg-Eppendorf, 20251 Hamburg, Germany
14 [2]Department of Chemosensation, Institute for Biology II, RWTH Aachen University, 52074
15 Aachen, Germany

16 [#]equal contribution

17
18 **Running title:** Early misconnectivity in a psychiatric risk model

19
20 *Corresponding authors: Ileana L. Hanganu-Opatz
21   hangop@zmnh.uni-hamburg.de
22
23
24
25
26
27 Figures: 6
28 Tables: 4
29 Multimedia: 1
30 Number of pages: 49
31 Number of words in Abstract: 216
32 Number of words in Introduction: 619
33 Number of words in Discussion: 1510

34
35 **Competing financial interest**
36 The authors declare no competing financial interests.

37

45

46   **Abstract**

47   Precise information flow from the hippocampus (HP) to prefrontal cortex (PFC) emerges

48   during early development and accounts for cognitive processing throughout life. On flip side,

49   this flow is selectively impaired in mental illness. In mouse models of psychiatric risk

50   mediated by gene-environment interaction (GE), the prefrontal-hippocampal coupling is

51   disrupted already shortly after birth. While this impairment relates to local miswiring in PFC

52   and HP, it might be also due to abnormal connectivity between the two brain areas. Here, we

53   test this hypothesis by combining *in vivo* electrophysiology and optogenetics with in-depth

54   tracing of projections and monitor the morphology and function of hippocampal afferents in

55   the PFC of control and GE mice of either sex throughout development. We show that

56   projections from the hippocampal CA1 area preferentially target layer 5/6 pyramidal neurons

57   and interneurons, and to a lesser extent layer 2/3 neurons of prelimbic (PL) subdivision of

58   PFC. In neonatal GE mice, sparser axonal projections from CA1 pyramidal neurons with

59   decreased release probability reach the PL. Their ability to entrain layer 5/6 oscillatory

60   activity and firing is decreased. These structural and functional deficits of hippocampal-

61   prelimbic connectivity persist, yet are less prominent in pre-juvenile GE mice. Thus, besides

62   local dysfunction of HP and PL, weaker connectivity between the two brain areas is present

63   in GE mice throughout development.

64   Keywords: development, prefrontal cortex, hippocampus, network oscillations, axonal

65   projections, mouse model of psychiatric risk, neuronal firing

66

67   **Significance Statement**

68   Poor cognitive performance in mental disorders comes along with prefrontal-hippocampal

69   dysfunction. Recent data from mice that model the psychiatric risk mediated by gene-

70   environment interaction identified the origin of deficits during early development, when the

71   local circuits in both areas are compromised. Here, we show that sparser and less efficient

72   connectivity as well as cellular dysfunction are the substrate of the weaker excitatory drive

73   from hippocampus to prefrontal cortex as well as of poorer oscillatory coupling between the

74   two brain areas in these mice. While the structural and functional connectivity deficits persist

75   during the entire development, their magnitude decreases with age. The results add

76   experimental evidence for the developmental miswiring hypothesis of psychiatric disorders.

Introduction

The brain circuitry accounting for memory and executive abilities in mammals is highly complex and extends over cortical and subcortical areas, yet two brain areas, hippocampus (HP) and prefrontal cortex (PFC), are considered as being its core (Bahner and Meyer-Lindenberg, 2017). Both areas are involved in memory processing: the HP controls episodic memory, whereas the PFC allows adaptive flexibility of memory processing (Spellman et al., 2015; Eichenbaum, 2017). The HP and PFC tightly interact to achieve memory retrieval and consolidation (Miller and Cohen, 2001; Preston and Eichenbaum 2013) via direct monosynaptic as well as indirect polysynaptic projections (Jay et al., 1989; Dolleman-Van Der Weel and Witter, 1996; Vertes, 2006). The highly efficient communication relevant for memory processing is mediated by oscillatory synchrony of neural activity in the two brain areas (Siapas et al., 2005; Backus et al., 2016; Alemany-Gonzalez et al., 2020). On the flip side, abnormal episodic memory, as one trait of a broader pattern of deficits in higher cognitive functions, has been reported for psychiatric disorders (Dere et al., 2010; Greenland-White et al., 2017). The cognitive impairment significantly contributes to disability and represents a major burden for patients because it is generally treatment refractory (Bora et al., 2010). Poor cognitive performance relates to reduced prefrontal-hippocampal connectivity in both schizophrenia patients, prodromal and high-risk subjects as well as mouse models of disease (Friston and Frith, 1995; Meyer-Lindenberg et al., 2005; Sigurdsson et al., 2010; Greenland-White et al., 2017). In line with the neurodevelopmental origin of schizophrenia, it has been hypothesized that, while the behavioral symptoms are firstly detectable in young adulthood, the underlying network is compromised at a much earlier stage (Owen et al., 2016).

Experimental confirmation of this hypothesis in human subjects faces major technical and ethical limitations. Therefore, animal models, despite being able to mimic only some disease features (e.g., etiology, neurochemical deficits, behavioral symptoms), are instrumental for uncovering the mechanisms of mental illness-related dysfunction (Nestler

104   and Hyman, 2010; Sigurdsson, 2016; Diamantopoulou and Gogos, 2019). Genetic models,

105   such as mice modeling 22q11.2 microdeletions identified in patients (McDonald-McGinn et

106   al., 2015) as well as models combining genetic deficits and environmental stressors related

107   to higher disease risk (dual-hit genetic-environmental (GE) models) (Kannan et al., 2013)

108   show cognitive impairment and abnormal communication within prefrontal-hippocampal

109   circuits (Sigurdsson et al., 2010). We previously showed that these deficits emerge already

110   early in life, at a developmental stage corresponding to neonatal period in mice (first

111   postnatal week) and third gestational trimester in humans (Clancy et al., 2001). Dual-hit GE

112   mice mimicking both the genetic (mutation of the intracellular hub of developmental

113   processes Disrupted-In-Schizophrenia 1 (DISC1) gene) (Brandon and Sawa, 2011) and the

114   environmental (challenge by maternal immune activation (MIA)) background that has been

115   related to mental illness, have abnormal patterns of early electrical activity both in PFC and

116   HP (Hartung et al., 2016; Xu et al., 2019; Chini et al., 2020; Xu et al., 2021). Additionally,

117   prefrontal-hippocampal coupling through synchrony of oscillatory activity as well as directed

118   HP-to-PFC interactions are diminished. Three mechanisms might cause these early deficits:

119   (i) local disruption of prefrontal circuits, (ii) local disruption of hippocampal circuits, and/or (iii)

120   abnormal long-range communication between PFC and HP. We previously confirmed the

121   first two mechanisms and reported that (i) layer 2/3 pyramidal neurons in PFC experienced

122   excessive microglia-induced synaptic pruning leading to impaired beta-gamma oscillations

123   (Chini et al., 2020) and (ii) the sharp-waves, firing, and network activity in hippocampal CA1

124   area are decreased in GE mice (Xu et al., 2021). Here, we address the third hypothesis and

125   investigate the long-range connectivity between HP and PFC throughout development in

126   dual-hit GE mice. We show that both structural and functional deficits of hippocampal

127   innervation of PFC compromise the communication between the two brain areas.

128   **Materials and Methods**

129   *Animals*

130 All experiments were performed in compliance with the German laws and the guidelines of

131 the European Community for the use of animals in research and were approved by the local

132 ethical committee (G17/015, N18/015). Timed-pregnant mice from the University Medical

133 Center Hamburg-Eppendorf animal facility were housed individually at a 12 h light/12 h dark

134 cycle and were given access to water and food ad libitum. The day of vaginal plug detection

135 was considered embryonic day (E) 0.5, the day of birth was considered postnatal day (P) 0.

136 The heterozygous offspring carrying a DISC1 allele (DISC1^{Tm1Kara}) on a C57BL/6J

137 background, whose dams were injected at E9.5 with the viral mimetic polyinosinic-

138 polycytidylic acid (poly I:C, 4 mg/kg, i.p.), were classified as dual-hit genetic-environmental

139 (GE) mice (Hartung et al., 2016). Pups born from homozygous Disc1^{Tm1Kara} dams and

140 wildtype males, and pups born from wildtype dams and homozygous Disc1^{Tm1Kara} males

141 were pooled together, as no difference between the two groups was found. Genotypes were

142 assessed using genomic DNA (tail biopsies) and the following primer sequences: forward

143 primer   5'-TAGCCACTCTCATTGTCAGC-3'   and   reverse   primer   5'-

144 CCTCATCCCTTCCACTCAGC-3'. Nontreated wildtype C57BL/6J mice and the offspring of

145 dams injected at E9 with saline (0.9%) were used as controls (CON) and combined together,

146 as no difference between the two groups was found. All experiments were performed on

147 pups of both sexes during neonatal development at P8–P10, as well as during pre-juvenile

148 development at P20–P24.

149 ***Stereotaxic injections***

150 The pups were placed in a stereotactic apparatus and kept under anesthesia with isoflurane

151 (induction: 5%, maintenance: 2.5%) for the entire procedure. For retrograde tracing,

152 fluorogold (FG, 2.5%, Fluorochrome, LLC, USA) was iontophoretically injected into the PFC

153 (0.5 mm anterior to bregma, 0.3 mm right to the midline) of P7 or P21 mice. For anterograde

154 tracing, biotinylated dextran amine (BDA, 5% in 0.125 M phosphate buffer, Thermo Fisher

155 Scientific, USA) was iontophoretically injected in the HP (0.7 mm anterior to lambda, 2.3 mm

156 right to the midline) of P7 or P21 mice. A glass capillary (~25 mm tip diameter) was filled

157 with ether ~1 µl FG or ~1 µl BDA by capillary forces, and a silver wire was inserted such that

158 it was in contact with the FG or BDA solution. For both anterograde and retrograde tracing,

159 the positive pole of iontophoresis device was attached to the silver wire, whereas the

160 negative one was attached to the skin of the neck. The capillary was carefully lowered into

161 the PFC (~1.5 mm dorsal from the dura) or HP (~1.5 mm dorsal from the dura). For

162 injections, anodal current to the pipette (6 s on/off current pulses of 6 mA) was applied for 10

163 min. For recordings of PL-projecting cells in CA1, a 0.5 µl syringe (Hamilton Company, Reno,

164 NV) was attached to a microsyringe pump controller (Micro4, WPI) and Alexa Fluor-555-

165 conjugated Cholera Toxin Subunit B (CTB, 1.0 mg/mL, 150 nl, 80 µl/min, Thermo Fisher

166 Scientific) was injected into the PL of P6 mice at the same coordinates as for FG injection.

167 For trans-synaptic labeling, a 0.5 µl syringe was attached to a microsyringe pump controller

168 and wheat germ agglutinin (WGA, 200 nl 4%, Vector Laboratories, Burlingame, CA) was

169 injected at a rate of 80 µl/min into the HP at the same coordinates as for BDA injection. For

170 all optogenetic experiments, the same procedure was used to inject AAV9-hSyn-

171 hChR2(H134R)-EYFP (Addgene, 2.67×10^{13} GC/µl) into the HP (80 nl, 50 nl/min for P1 mice

172 and 150 nl, 80 nl/min for P13-P15 mice). Following injection, the pipette or syringe was left in

173 place for at least 5 min to allow optimal diffusion of the solution. The scalp was closed by

174 application of tissue adhesive glue. The pups were warmed on a heating pad for 10–15 min

175 and returned to the dam until full recovery of the motor activity. The pups were perfused 3

176 days later for FG and BDA staining. The perfusion occurred 30 h after WGA injection, in line

177 with literature and our pilot data that showed trans-synaptic transfer to the 1st order but no

178 other downstream neurons (Phillips et al., 2019). All the WGA-positive cells were co-stained

179 with NeuN to exclude the possibility of non-neuronal innervation (data not shown).

180 ***In utero electroporation and clearing***

181 Timed-pregnant CON or GE mice (E15.5) were injected subcutaneously with buprenorphine

182 (0.05 mg/kg body weight) 30 min before surgery. Surgery was performed on a heating

183 blanket, and toe pinch and breathing were monitored throughout. Under isoflurane

184   anesthesia (induction: 5%, maintenance: 3.5%), the eyes of the dam were covered with eye

185   ointment to prevent damage before the uterine horns were exposed and moistened with

186   warm sterile phosphate buffered saline (PBS, 37°C). Solution containing 1.25 µg/µl pAAV-

187   CAG-tDimer2 and 0.1% fast green dye at a volume of 0.75-1.25 µl was injected into the right

188   lateral ventricle of individual embryos using pulled borosilicate glass capillaries with a sharp

189   and long tip. Plasmid DNA was purified with NucleoBond (Macherey-Nagel, Germany). To

190   target intermediate and ventral HP (i/vHP), a tri-polar approach was used (Szczurkowska et

191   al., 2016). Each embryo within the uterus was placed between the electroporation tweezer-

192   type paddles (5 mm diameter, both positive poles, Protech, TX, USA) that were oriented at a

193   90° leftward angle from the midline and a 0° angle downward from anterior to posterior. A

194   third custom build negative pole was positioned on top of the head roughly between the eyes.

195   Electrode pulses (30 V, 50 ms) were applied six times at intervals of 950 ms controlled by an

196   electroporator (CU21EX, BEX, Japan). Uterine horns were placed back into the abdominal

197   cavity after electroporation. The abdominal cavity was filled with warm sterile PBS (37°C)

198   and abdominal muscles and skin were sutured individually with absorbable and non-

199   absorbable suture thread, respectively. After recovery, pregnant mice were returned to their

200   home cages, which were half placed on a heating blanket for two days after surgery, and

201   received on a daily basis additional wet food supplemented with 2-4 drops Metacam (0.5

202   mg/ml, Boehringer-Ingelheim, Germany).

203   Fluorescence expression was confirmed at P2 using a portable fluorescence

204   flashlight (Nightsea, MA, USA). At P10, pups were anesthetized with 10% ketamine

205   (aniMedica, Germany) / 2% xylazine (WDT, Germany) in 0.9% NaCl solution (10 µg/g body

206   weight, intraperitoneally) and transcardially perfused with Histofix (Carl Roth, Germany)

207   containing 4% paraformaldehyde. Brain clearing was performed as previously described

208   (Chung and Deisseroth, 2013). Brains were postfixed overnight at 4°C to maintain structural

209   integrity in hydrogel fixation solution containing 4% acrylamide, 0.05% bis-acrylamide, 0.25%

210   VA-044 Initiator, 4% PFA in PBS$^{-/-}$. To allow hydrogel polymerization, oxygen was removed

211   via a vacuum pump connected to a desiccator. Argon was released and removed twice to

212   establish O_2-free conditions. After heat-triggered polymerization (37°C; 3 h), samples were

213   extracted from hydrogel and washed in a clearing solution containing 200 mM boric acid and

214   138 mM SDS (pH 8.5) for 24 h at room temperature (RT). Embedded brains were cleared at

215   37°C for 48 days. Clearing solution was changed twice each week. DRAQ5 (nuclear marker;

216   1:1000) was added for 2 days. Next, removal of SDS (washing (3x) in PBST (0.1% TritonX in

217   PBS$^{-/-}$) at RT) terminated clearing. Imaging was performed after 24 h incubation in RIMS80

218   containing 80 g Nycodenz, 20 mM PS, 0.1% Tween 20, and 0.01% sodium acid. Imaging

219   was performed with a Cleared tissue LightSheet (Intelligent Imaging Innovations, Inc.,

220   Denver CO) dual-side illumination lightsheet microscope for whole organ imaging, equipped

221   with a PlanNeoFluar 1.0x / 0.25NA objective. 3D stacks were acquired sequentially. A 640

222   nm laser was used for excitation of DRAQ5 using a multi-line Set 43HE filter cube and a 561

223   nm laser for tDimer Ds-Red Filter cube. Image stacks were stitched using slidebook 6

224   software. Brain regions of interest were manually marked using nuclear staining by

225   inspecting coronal slices of the 3D dataset using Imaris 9.7. Fibers were reconstructed and

226   fiber volume within the prelimbic cortex was calculated. The fiber volume / PL volume ratio

227   was normalized to the transfected cell count in the lateral hippocampal region.

228   ***Electrophysiological recordings and optogenetic manipulation in vivo***

229   Multisite extracellular recordings were performed in the prelimbic subdivision (PL) of the PFC

230   from P8-10 or P20-P24 mice. For recordings in non-anesthetized state in P8-P10 mice, 0.5%

231   bupivacaine / 1% lidocaine was locally applied on the neck muscles. For recordings in

232   anesthetized state in P20-P24 mice, mice were injected intraperitoneally with urethane (1

233   mg/g body weight; Sigma-Aldrich) before surgery. For both groups, the surgery was

234   performed under isoflurane anesthesia (induction: 5%; maintenance: 1.5-2%). The head of

235   the pup was fixed into a stereotaxic apparatus using two plastic bars mounted on the nasal

236   and occipital bones with dental cement. The bone over the PFC (0.8 mm anterior to bregma,

237   0.1-0.5 mm right to the midline) and the CA1 area of the i/vHP (0.8-1.0 mm anterior to

238   lambda, 3.5-3.8 mm right to the midline) was carefully removed by drilling holes of 0.5 mm

239   diameter. Four-shank optoelectrodes with 4 × 4 recording sites (0.4-0.8 MΩ impedance, 0.1

240   mm spacing, 0.125 mm inter-shank spacing; NeuroNexus, MI, USA), aligned with optical

241   fibers (50 μm diameter) and ending 200 μm above the top recording sites, were inserted into

242   PL at a depth of 2.0 mm from the skull surface. One silver wire was inserted into cerebellum

243   to serve as ground and reference electrode. Before signal acquisition, a recovery period of

244   15 min after electrode insertion was provided. In PL, the two medial shanks were located

245   into layer 2/3, whereas the lateral shanks were located into layer 5/6. Extracellular signals

246   were band-pass filtered (0.1 Hz to 5 kHz) and digitized (32 kHz) with a multichannel

247   extracellular amplifier (Digital Lynx SX, Neuralynx) and the Cheetah acquisition software

248   (Neuralynx).

249   Pulsatile (laser on-off, 5 ms, 8 Hz, 3 s) or ramp (linearly increasing power, 3 s) light

250   stimulations *in vivo* were performed with an Arduino uno (Arduino, Italy) controlled laser

251   system (473 nm wavelength, Omicron, Austria), which was coupled with a 50 μm (four-

252   shank electrodes) diameter light fiber (Thorlabs, NJ, USA). Each type of stimulation was

253   repeated 60 times with an interval of 7 s. Laser power was measured and adjusted to the

254   range of 0.75-2.5 mW at the fiber tip.

255   ***Electrophysiological recordings and optogenetic manipulation in vitro***

256   For patch-clamp recordings, pups were anaesthetized with 5% isoflurane and decapitated.

257   Brains were rapidly removed and placed in ice-cooled oxygenated (95% O_2/5% CO_2) high-

258   sucrose-based artificial cerebral spinal fluid (ACSF) containing (in mM): 228 sucrose, 2.5

259   KCl, 1 NaH_2PO_4,1 26.2 $NaHCO_3$, 11 glucose and 7 $MgSO_4$ (310 mosmol/kg H_2O). Coronal

260   brain slices (300 μm) were prepared using a vibratome (Leica VT 1000S). Slices were

261   allowed to recover in oxygenated ACSF containing (in mM): 119 NaCl, 2.5 KCl, 1 NaH_2PO_4,

262   26.2 $NaHCO_3$, 11 glucose, 1.3 $MgSO_4$ (310 mOsmol/kg H_2O) at 33 °C for at least 30 min,

263   then kept at room temperature (~22 °C) for at least another 60 min before recordings. Slices

264   were transferred to the recording chamber and continuously perfused with oxygenated

265   standard ACSF (2–3 mL/min) at room temperature.

266   Whole-cell recordings were made from neurons located in PL and HP. The location

267   and neuronal morphology served to identify the prelimbic layers. PL-projecting neurons in

268   CA1 of i/vHP were identified by CTB555 labeling after tracer injection into PL. Two to three

269   coronal slices were used per animal and chosen according to the coordinates relative to

270   Bregma (for PL, AP: +1.70 to +0.7 mm; for HP, -3.0 to -4.0 mm). Slices were visualized

271   using an upright microscope (BX50WI, Olympus Optical, Tokyo, Japan) and with infrared

272   and differential interference contrast optics. All recordings were performed from pyramidal

273   neurons identified according to their shape, spiking pattern, and action potential width.

274   Borosilicate glass patch pipettes (4-8 MΩ) were filled with K-gluconate-based solution

275   containing (in mM): 130 K-gluconate, 10 Hepes, 0.5 EGTA, 4 Mg-ATP, 0.3 Na-GTP, 8 NaCl

276   (285 mosmol/kg H_2O, pH adjusted to 7.4 with KOH) and 0.3%-0.5% biocytin for post hoc

277   morphological identification of recorded cells. Recordings were performed with an EPC 10

278   amplifier and PatchMaster software v2x73.1 (HEKA Elektronik), filtered at 2.9 kHz using a

279   Bessel filter, and sampled at 10 kHz. All potentials were corrected for the liquid junction

280   potential of the gluconate-based electrode solution, which, according to our measurement,

281   was −8.65 mV. The resting membrane potential (RMP) was measured immediately after

282   obtaining the whole-cell configuration. Unless otherwise noted, all experiments were carried

283   out at a membrane potential of -70 mV under voltage clamp conditions. To measure the

284   basic properties of the membrane, 600 ms long hyperpolarizing or depolarizing current

285   pulses ranging from -100 pA to 120 pA in a 20 pA step were applied. Access resistance (R_s)

286   was monitored under voltage-clamp conditions by analyzing capacitive transients during 5

287   ms-long square wave depolarizing pulses. Recordings were included only when a GΩ seal

288   formed prior to whole-cell access with R_s of less than 30 MΩ. Cells with R_s changes > 25%

289   were excluded from further investigation. Spontaneous excitatory postsynaptic current

290   (EPSC) events were recorded at a holding potential of -70 mV. None of the investigated

291   neurons showed spontaneous firing at resting membrane potential.

292   For optogenetic stimulation *in vitro*, 470-nm light pulses were applied with a CoolLED

293   system (pE-2) attached to the upright microscope. Maximal light output at 470 nm was

11

294   measured at 2 mW with an optical power meter (Thorlabs, NJ, USA). For stimulation of

295   hippocampal afferents targeting prelimbic neurons, light pulses (3 ms, 5 ms 10 ms, 15 s

296   interval) were repetitively applied every 15 s for up to 10 times. For the investigation of short-

297   term synaptic plasticity, train pulses consisted of 2 s-long light pulses at 2 Hz, 4Hz, 8 Hz

298   repeated every 15 s for up to 5 times. The induced EPSCs and inhibitory postsynaptic

299   current (IPSCs) were voltage-clamp recorded at -70 mV and +10 mV, respectively. To block

300   AMPA/kainate receptors, 10 µM CNQX (6-cyano-7-nitroquinoxaline-2, 3-dione) was added

301   to the recording chamber solution.

302   ***Histology and immunohistochemistry***

303   Briefly, P8–P10 and P20–P24 mice were anesthetized with 10% ketamine / 2% xylazine in

304   0.9% NaCl solution (10 µg/g body weight, i.p.) transcardially perfused with Histofix

305   containing 4% PFA. Brains were postfixed with 4% PFA for 24 h and sectioned coronally at

306   100 µm for reconstruction of the position of electrodes, or 50 µm for further staining.

307   Sections for staining were collected in three equally spaced series. To reduce the

308   redundancy of information of neighbor slices, only one of the series was mounted or used for

309   subsequent staining and analysis.

310   For immunohistochemistry, free floating slices were permeabilized and blocked with

311   PBS containing 0.3% Triton X-100 (Sigma Aldrich), 5% normal bovine serum (Jackson

312   ImmunoResearch). Subsequently, slices were incubated overnight with mouse monoclonal

313   Alexa Fluor-488-conjugated antibody against NeuN (1:100, MAB377X; Merck Millipore, MA,

314   USA), Alexa Fluor-488-conjugated streptavidin (1:1000, Merck Millipore), or rabbit polyclonal

315   primary antibody against GABA (1:1000, no. A2052; Sigma-Aldrich), polyclonal guinea-pig

316   antibody against VGLUT1 (1:1000, Synaptic Systems, Germany), rabbit polyclonal primary

317   antibody against lectin (1:1000, no. A2052; Sigma-Aldrich) followed by 2 h incubation with

318   Alexa Fluor-568 goat anti-rabbit IgG secondary antibody (1:500, A11008; Merck Millipore),

319   Alexa Fluor-568 goat anti-guinea pig (1:500, Molecular Probes, OR, USA), Alexa Fluor-568

320   donkey anti-rabbit (1:500, Life Technologies, CA, USA) and Alexa Fluor-568-conjugated

321   streptavidin (1:1000, Merck Millipore). DAPI (1:500) was added to the second antibody for

322   the nuclear labeling. Finally, slices were transferred to glass slides and covered with Vecta-

323   Shield (Vector Laboratories). To avoid cross-reactivity between the anti-lectin primary

324   antibody and other antibodies, sections were firstly incubated with anti-lectin and then

325   underwent subsequent biotinylation and streptavidin treatment steps. Following the last

326   wash, sections were again blocked for 2 h.

327   For BDA staining, sections (prepared as described above) were rinsed in PBS (0.125

328   M, pH 7.4–7.6) for 10 min, treated with peroxide solution (3% peroxide, 10% methanol in

329   0.125 M PB) for 10 min to quench any endogenous peroxidases within the tissue, and rinsed

330   again in PB three times for 10 minutes each. Subsequently, the sections were washed in

331   PBS containing 0.5% Triton-X and incubated with avidin biotinylated enzyme complex

332   (Vectastain ABC kit; Vector, Burlingame, CA) at room temperature (90 min) or overnight at

333   4°C according to the manufacturer's instructions. After rinsing in Tris-HCl (pH 7.4), the

334   sections were further incubated with DAB working buffer (DAB peroxidase substrate kit,

335   Vector Laboratories, USA) at room temperature for 2–10 min. After the signal was detected,

336   all sections were rinsed with Tris-HCl, mounted on slides, dehydrated, cleared in xylenes,

337   coverslipped, and viewed with brightfield microscopy. In some cases, nuclear staining was

338   necessary to aid the delineation of brain regions.

339   *Imaging*

340   Wide-field fluorescence was performed to reconstruct the position of recording electrode in

341   brain slices of investigated pups. For DAB staining, all bright field images were obtained

342   using a Zeiss imager M1 microscope (Zeiss, Oberkochen, Germany) with identical settings.

343   Bright field photomicrographs were imported into FIJI and their contrast and brightness were

344   adjusted. Axons were manually traced using FIJI. Area and layer borders were set by

345   superimposing photomicrographs of BDA sections with another series of sections that

346   processed for nuclear staining. Hippocampus was stained with streptavidin and DAPI,

347   injection sites in hippocampus were examined and the number of injected neurons was

348   counted. The number of stained neurons was averaged over three hippocampal slices

349   (every third 50 μm-thick slices from the series containing the HP). The density of

350   hippocampal axons ($\mu m/mm^2$) in the PL was normalized to the number of stained neurons in

351   the CA1 and the values were given as $\mu m/mm^2/cell$. In the retrograde tracing experiment, all

352   fluorogold-positive cells in the CA1 were quantified automatically using custom-written

353   algorithms in FIJI, and confirmed by visual inspection. Subsequent analyses of tracing were

354   performed at animal level.

355   ***Data Analysis***

356   Electrophysiological data were imported and analyzed offline using custom-written tools in

357   MATLAB software version 7.7 (Mathworks). Data were band-pass filtered (500–5000 Hz for

358   spike analysis or 1–100 Hz for local field potentials (LFP)) using a third-order Butterworth

359   filter forward and backward to preserve phase information before down-sampling to 1000 Hz

360   to analyze LFP.

361   *Power spectral density*. For power spectral density analysis, 1 s-long windows of network

362   oscillations were concatenated and the power was calculated using Welch's method with

363   non-overlapping windows. For optical ramp stimulation, we compared the average power

364   during the 1.5 s-long time window preceding the stimulation to the last 1.5 s-long time

365   window of light-evoked activity.

366   *Single unit activity (SUA)*. SUA was detected and clustered using klusta (Rossant et al.,

367   2016) and manually curated using phy (https://github.com/cortex-lab/phy). Data were

368   imported   and   analyzed   using   custom-written   tools

369   (https://github.com/OpatzLab/HanganuOpatzToolbox) in MATLAB.

370   *Firing rate*. The firing rate was computed by dividing the total number of spikes by the

371   duration of the analyzed time window. For optical pulsatile stimulations, modulation index (MI)

372   of firing rate was calculated as ($Firing_{during-stimulation}$ - $Firing_{pre-stimulation}$) / ($Firing_{during-stimulation}$ +

373    $Firing_{pre-stimulation}$).

374   *Membrane properties.* Analysis of data resulted from patch-clamp recordings was performed

375   offline using custom-written scripts in MATLAB. For all recorded neurons, RMP, input

376   resistance (R_{in}), membrane time constant (τ_m), membrane capacity (C_m), R_s, action potential

377   (AP) amplitude, halfwidth, and firing threshold were calculated. R_{in} was calculated according

378   to Ohm's law by dividing the resulting potential changes by the amplitude of the applied

379   current (-60 pA). τ_m was calculated by fitting a monoexponential function to the induced

380   potential deflection. C_m was calculated by dividing τ_m by R_{in}. Firing threshold voltage was

381   considered at the point where the depolarization speed firstly exceeded 10 mV/ms. Action

382   potential amplitude was measured from threshold to peak, with the half-width measured at

383   half this distance. Firing rate was calculated during a 600 ms-long depolarization of the cells

384   by 80 pA current injection. Sag amplitude was calculated for each cell as the proportional

385   difference between the initial voltage response (i.e., during the first 200 ms of the current

386   pulse) and the steady state response (averaged for 100 ms) to a hyperpolarizing current

387   pulse of -100 pA. Data from PL-projecting neurons and randomly selected neurons in CA1 of

388   i/vHP were pooled together, since no significant differences in the passive and active

389   membrane properties were detected between the two groups.

390   *Synaptic activity.* Synaptic events were automatically detected automatically on template

391   parameters (Pernia-Andrade et al., 2012) and manually examined to exclude false positive

392   events. Events were excluded if the amplitude was < 3 pA. Inter-event interval (event

393   frequency) and event amplitude were analyzed and compared between groups. Light-

394   evoked EPSCs (eEPSCs) were averaged over 10-20 stimuli. Their peak amplitude and

395   onset (i.e., delay between light stimulus and time point at which the response speed

396   exceeded 10 pA/ms) were calculated. The coefficient of variation (CV) for a given measured

397   variable was defined as the ratio between the standard deviation and the average value of

398   10-20 individual responses to light stimulation.

399   *Statistics.* Statistical analyses were performed in MATLAB environment. Data were tested for

400   significant differences using one-way repeated-measures analysis of variance (ANOVA)

401   followed with Bonferroni-corrected post hoc analysis. Data with non-normal distribution (only

402   the eEPSC amplitude) were tested with the nonparametric ANOVA followed by Bonferroni-

403   corrected post hoc analysis. The effect of experimental groups and layers on the properties

404   of sEPSC was tested using two-way ANOVA followed by Bonferroni-corrected post hoc

405   analysis. Values were considered outliers and removed when their distance from the 25th or

406   75th percentile exceeded 1.5 times the interquartile interval. Data are presented as mean ±

407   SEM. Significance levels of $p < 0.05$ (*), $p < 0.01$ (**) or $p < 0.001$ (***) were used.

408   **Results**

409   ***Anatomical characterization of hippocampal projections targeting the prelimbic cortex***

410   ***in control and dual-hit GE mice***

411   To gain insight into prefrontal-hippocampal communication during development in dual-hit

412   GE mice, we first performed an in-depth structural analysis of axonal projections that link the

413   two regions. In adult mice, the prelimbic subdivision of medial PFC (PL) and hippocampus

414   (HP) interacts along multiple multi-synaptic routes. The main route of communication is the

415   dense ipsilateral monosynaptic projection from HP to PL, lacking a feedback equivalent (Jay

416   and Witter, 1991; Cenquizca and Swanson, 2007). However, the developmental profile of

417   these unidirectional projections is still poorly understood.

418   To close this knowledge gap, we performed retrograde and anterograde staining of

419   the hippocampal projections accompanied by path tracking during early neonatal

420   development (Fig. 1A). First, we used the retrograde tracer Fluorogold (FG) that was

421   iontophoretically injected into the PL of control mice (CON) (n=4) at postnatal day (P) 7.

422   Three days later, we detected labeled neurons in PL (Fig. 1B), with minimal diffusion to

423   neighboring areas, such as infralimbic cortex (IL). FG injection labeled few cells in dorsal HP

424   (dHP), but labeled cell density augmented along the fronto-caudal axis and peaked at the

425   level of intermediate and ventral HP (i/vHP), which is consistent with our previous results

426   (Ahlbeck et al., 2018). FG-positive neurons were not uniformly distributed over hippocampal

427   areas but mainly concentrated in the deep layers of CA1 region, close to *stratum oriens* (SO)

428   (Fig. 1B). Second, we iontophoretically injected the anterograde tracer biotinylated dextran

429   amine (BDA) into the hippocampal CA1 region of P7 CON mice (n=7) (Fig. 1C). Three days

430   later, BDA-labeled axonal terminals were detected in PL, accumulating in, yet not exclusively

431   restricted to layer 5/6. The path and distribution of hippocampal axonal streamlines

432   terminating in PL were revealed in whole-brain imaging after electrophoretic tissue clearing

433   and confocal fluorescence microscopy (Fig. 1D, Multimedia 1). These results show that

434   already at neonatal age, the distribution of axonal projections over prelimbic layers

435   resembles connectivity previously described for adult mice (Parent et al., 2010; Padilla-

436   Coreano et al., 2016; Liu and Carter, 2018). The BDA-positive terminals had large boutons

437   (Fig. 1E) and were vGLUT1 immunopositive (Fig. 1E), indicating that hippocampal

438   projections targeting PL are glutamatergic. They seem to target both interneurons and

439   pyramidal neurons, as shown by close proximity of BDA-stained axons to both GABA-

440   positive and -negative cells (Fig. 1E). To confirm these results and identify first-order

441   postsynaptic neurons in PL innervated by hippocampal axons, we injected the trans-synaptic

442   marker wheat germ agglutinin (WGA) into the HP of CON mice (n=3). WGA-positive

443   postsynaptic neurons have been identified in both layer 5/6 and layer 2/3 of PL (Fig. 1F).

444   GABA co-staining showed that the large majority (97.9 %, 423 out of 432) of WGA-positive

445   neurons were GABA-negative and very few targeted neurons (2.1 %, 9 out of 432) were

446   GABA-positive (Fig. 1F). These results indicate that, already at the end of the first postnatal

447   week, hippocampal neurons located in *stratum oriens* of CA1 area project to PL, where they

448   mainly, but not exclusively, target pyramidal neurons.

449   In dual-hit GE mice (n=7), the overall pattern of hippocampal innervation in PL was

450   similar to that identified in neonatal CON mice. However, when monitoring the density of

451   axonal projections from i/vHP to PL major differences were detected between the two groups.

452   In cleared brains, fewer projections were visualized and quantified in the PL of neonatal GE

453   mice when compared to CON mice (Fig. 1D, inset). This was confirmed after BDA staining.

454   Fewer projections have been detected in the deeper prelimbic layers of neonatal GE mice

455   (n=7 mice) than CON mice (n=7 mice) (in $\mu m/mm^2$/cell, CON: 53.07 ± 9.41; GE: 22.67± 3.76;

456    $F_{(1,12)}=9.00$, p=0.011) (Fig. 1G). In contrast, the density of hippocampal projections in the

457 upper layers of PL was similar (in µm/mm^2/cell, CON: 10.79 ± 3.17; GE: 8.57 ±4.31;

458 F(1,12)=0.17, p=0.686) in all investigated mice, yet these layers are not the major target of

459 CA1 innervation and therefore, the overall density here was low (Fig. 1G). Thus, sparser

460 connectivity from HP to PL is present in neonatal GE mice.

461   These connectivity deficits persisted during the entire development, as shown by the

462 results of similar BDA injections in the i/vHP of P21 pre-juvenile GE and CON mice (Fig. 1H).

463 At P24, the density of hippocampal projections, especially in deeper prelimbic layers,

464 strongly increased in all mice, yet it was still smaller (in µm/mm^2/cell, CON layer 5/6:

465 153.27±30.11; GE layer 5/6: 58.26 ± 12.03; F(1,19)=7,969, p=0.0108, Fig. 1H) in GE mice

466 (n=10 mice) when compared to CON mice (n=11 mice). In contrast, no differences between

467 the groups were detected for the rather sparse innervation of prelimbic layer 2/3 (in

468 µm/mm^2/cell, CON: 50.08 ± 11.57; GE: 39.41 ± 16.93; F(1,19)=0.280, p=0.603).

469   To answer the question of whether the sparser hippocampal innervation of layer 5/6

470 in GE mice relates to fewer projecting neurons in CA1 area or cropped arborization of

471 projections, we injected the retrograde tracer FG into PL (CON: n=4 mice, GE: n=4 mice)

472 and quantified the density of stained hippocampal neurons (Fig. 1I, J). The density of PL-

473 projecting neurons was significantly lower in neonatal GE mice when compared to CON (in

474 *10000/mm^2, CON: 2.59 ± 0.414; GE: 1.24 ± 0.28; F(1,6)=7.20, p=0.0364). In contrast, the

475 density of retrogradely stained CA1 neurons was similar in CON (n=4 mice) and GE (n=5

476 mice) mice at pre-juvenile age (in *10000/mm^2, CON: 2.13 ± 0.16; GE: 2.47 ± 0.45,

477 F(1,7)=0.409, p=0.543). A similar density of PFC-projecting neurons but a lower density of

478 hippocampal projections in PL suggests that the projections are less arborized in pre-

479 juvenile GE mice.

480   These data show that the hippocampal innervation of PL is impaired in GE mice, with

481 fewer CA1 neurons projecting to PL at neonatal age and less arborized projections towards

482 the end of pre-juvenile development.

483   ***Region- and age-dependent cellular dysfunction within hippocampal-prelimbic***

484   ***circuits of dual-hit GE mice***

485   The structural deficits observed in dual-hit GE mice along development lead to the question

486   of whether early neuronal function is affected as well. Abnormal cellular activity might

487   underlie the decreased functional communication between PL and HP that has been

488   previously reported in these mice at neonatal age (Hartung et al., 2016; Xu et al., 2019).

489   To test this hypothesis, we first monitored the membrane properties of prelimbic and

490   hippocampal CA1 neurons in neonatal (P8-10) and pre-juvenile (P20-24) CON and GE mice.

491   For this, we performed whole-cell patch-clamp recordings from visually identified and

492   biocytin-stained neurons in coronal slices including PL or i/vHP. In the PL, cells in the upper

493   layers (i.e., layer 2 and 3) as well as deeper layers (i.e., layer 5 and 6) have been recorded.

494   The pyramidal shape and the orientation of dendrites monitored post-mortem after biocytin

495   staining served as criteria to unequivocally classify the investigated cells as pyramidal

496   neurons (Fig. 2A, G). Already at neonatal age, the passive and active membrane properties

497   of prelimbic pyramidal neurons differed between neonatal CON and GE mice (CON layer 5/6:

498   n=33 cells, GE layer 5/6: n=20 cells, CON layer 2/3: n=27 cells, GE layer 2/3: n=14 cells).

499   The resting membrane potential (RMP) of upper layer neurons was more depolarized, the

500   AP amplitude smaller, and the AP halfwidth longer in GE when compared to CON mice

501   (Table 1). All neurons fired overshooting action potentials (APs) in response to sustained

502   depolarization by intracellular current injection (Fig. 2B). No difference in firing rate in

503   response to depolarizing current injection was detected between CON and GE (Fig. 2C).

504   With ongoing maturation, the cellular properties of prelimbic neurons evolved in all mice

505   (CON layer 5/6: n=57 cells, GE layer 5/6: n=23 cells, CON layer 2/3: n=15 cells, GE layer

506   2/3: n=9 cells, Fig. 2D). The differences between CON and GE mice diminished with age,

507   solely the RMP of prelimbic layer 2/3 pyramidal neurons being more hyperpolarized in pre-

508   juvenile GE mice when compared to CON (Table 1).

509   Second, we performed voltage-clamp recordings at a holding potential of -70 mV

510   from prelimbic neurons from neonatal CON and GE mice to assess their synaptic inputs (Fig.

511 2E, F). Spontaneous excitatory postsynaptic currents (sEPSCs) with large amplitude and

512 fast kinetics were recorded in prelimbic neurons from both groups. The occurrence (Fig. 2Eii)

513 but not amplitude (Fig. 2Eiii) of sEPSCs in prelimbic layer 2/3 was significantly smaller in GE

514 mice (Table 2). The synaptic activity in both areas was comparable between groups in pre-

515 juvenile CON and GE mice and only a few differences were detected (Fig. 2F, Table 2).

516 These data confirm previous investigations that detected prominent dysfunction within local

517 circuits and morphological change in the upper prelimbic layers in neonatal GE mice, and

518 less prominent changes in pre-juvenile GE mice (Chini et al., 2020).

519 Similar investigation of pyramidal neurons in CA1 area of i/vHP showed that their

520 passive and active membrane properties differed between neonatal CON (n=34) and GE

521 neurons (n=27). While the RMP and membrane capacitance values were similar among

522 groups, the input resistance was significantly smaller and the time constant shorter for CA1

523 neurons of GE mice (Table 1), suggesting lower excitability of these neurons when

524 compared to those from CON mice. This difference is supported by the bigger voltage sag

525 recorded upon hyperpolarization in hippocampal neurons from GE mice (Fig. 2H, Table 1).

526 The voltage sag mirrors activation of hyperpolarization-activated cyclic nucleotide-gated

527 (HCN) channels that are known to control neuronal excitability (Brennan et al., 2016). The

528 firing rate in response to sustained depolarization was similar in CON and GE mice (Fig. 2I,

529 Table 1). Solely the AP width was higher in neurons from GE mice. At pre-juvenile age, no

530 major differences in membrane properties and firing rate of hippocampal neurons were

531 detected between CON and GE mice (Fig. 2J, n=12 for CON, n=9 for GE, Table 1).

532 These data indicate that a mild cellular dysfunction of prefrontal and hippocampal

533 neurons is present in neonatal GE mice and diminishes with age.

534 ***Weaker efficiency of hippocampal drive to prelimbic cortex in neonatal dual-hit GE***

535 ***mice***

536   To investigate whether, besides structural disruption, the functional connectivity between HP

537   and PL is compromised in GE mice during development, we monitored the responsiveness

538   of prelimbic neurons to the activation of hippocampal terminals.

539   In a first step, we focused on cellular processes assessed under *in vitro* conditions.

540   For this, we selectively transfected pyramidal neurons in the HP of P1 CON and GE mice

541   with ChR2 (H134R) and fluorescent protein EYFP (AAV9-hSyn-hChR2(H134R)-EYFP) by

542   micro-injections (Fig. 3Ai). Whole-cell patch-clamp recordings from pyramidal CA1 neurons

543   in coronal slices including i/vHP from P8-10 mice confirmed that blue light (473 nm, 3 ms)

544   pulses reliably evoked APs (Fig. 3Aii-iii). In line with the results of morphological

545   investigations, fluorescent axonal terminals of transfected CA1 neurons were detected in the

546   deep and, to a lesser extent, in upper layers of PL (Fig. 3Bi). We performed voltage-clamp

547   recordings from visually-identified prelimbic pyramidal neurons and non-pyramidal cells (i.e.,

548   putatively interneurons) located in the proximity of terminals during light-stimulation of

549   hippocampal axons (Fig. 3Bii). Single pulses of light stimulation evoked prominent excitatory

550   postsynaptic currents (eEPSCs) in both pyramidal neurons (Fig. 3Ci) and interneurons (Fig.

551   3Cii), the amplitude of which augmented with increasing stimulus duration (3 ms: 24.81 ±

552   6.70 pA, 5 ms: 42.19 ± 9.02 pA, 10 ms: 63.6 ± 12.12 pA, $F_{(2,69)}=8.07$, p=0.017, p=0.012,

553   n=24) (Fig. 3Biii). The eEPSCs recorded from pyramidal neurons had a short latency and

554   fast kinetics and were fully abolished when ionotropic AMPA/kainate receptor antagonists

555   CNQX (10 µM) was added to the extracellular solution (Fig. 3Ci). Upon depolarization, the

556   AMPA receptor-mediated events were accompanied by a delayed di-synaptic postsynaptic

557   current.

558   While light stimulation evoked robust responses in prelimbic neurons of all

559   investigated pups (Fig. 3D), detailed analysis examining eEPSCs properties revealed

560   differences between CON and GE mice (Table 3). In both prelimbic layers in GE mice, fewer

561   neurons responded to light stimulation of hippocampal projections (layer 5/6, 41.67%; layer

562   2/3, 44.44%) when compared to responding neurons in CON (layer 5/6, 82.76%, p=0.0048;

563   layer 2/3, 80.76%, p=0.029). Moreover, the eEPSC evoked in layer 5/6 neurons had not only

564   smaller amplitude in GE vs. CON mice (63.6 ± 12.12 vs. 9.72 ± 2.41 pA, p=0.0009) but also

565   showed a higher degree of variability upon light stimulus as mirrored by the larger coefficient

566   of variation (CV) (Fig. 3Ei, ii, Table 3). The kinetics of eEPSCs were also disrupted in GE

567   mice, the events having a delayed onset (5.15 ± 0.476 vs 7.99 ± 0.762 ms, p=0.006) and

568   longer rise-time (3.07 ± 0.044 vs 3.60 ± 0.301 ms, p= 0.022) (Fig. 3Eiii, iv). In contrast, the

569   properties of light-evoked EPSCs in layer 2/3 neurons were similar for all investigated mice

570   (Fig. 3E, Table 3). The function of hippocampal terminals in PL was further assessed by

571   repetitive stimulation (Fig. 3Fi). All prelimbic neurons of neonatal CON and GE neurons

572   responded with a substantial depression of eEPSCs when normalized to the first event (Fig.

573   3Fii). However, the paired-pulse ratio (PPR), a measure of short-term plasticity (STP), for

574   layer 5/6 neurons in GE mice significantly decreased when the stimulation was delivered at a

575   500 ms interval (0.67 ± 0.057 vs. 0.21 ± 0.106, p= 0.0083) (Fig. 3G, Table 3). These results

576   suggest that the hippocampal inputs are less efficient on prelimbic neurons in GE mice.

577   To directly test this hypothesis, we investigated the impact of hippocampal inputs on

578   the oscillatory entrainment of local circuits in the PL of CON and GE mice *in vivo*. For this,

579   multi-site extracellular recordings of local field potential (LFP) and multiunit activity (MUA)

580   were performed in prelimbic layer 5/6 and layer 2/3 of P8-10 CON (n=14) and GE mice

581   (n=11) before, during and after repetitive stimulation with ramp light stimuli or pulse trains

582   (Fig. 4A). In line with our previous results, the used light intensity (0.75-2.5 mW) led to a

583   temperature increase of max. 0.2 °C, which is far below the local tissue heating that might

584   interfere with neuronal spiking (Stujenske et al., 2015; Bitzenhofer et al., 2017). Ramp

585   stimulation (3 s) significantly augmented theta band (4-12 Hz) oscillatory power in layer 5/6

586   of CON but not GE mice (0.807 ± 0.121 vs. 0.218 ± 0.096, F(1,23)=3.365, p=0.039) (Fig. 4B,

587   Table 4). Similarly, the magnitude of LFP response to light pulse trains (5 ms-long, 8 Hz,

588   total duration of a train 3 s) significantly differed between the two groups (Fig. 4C). Activation

589   of hippocampal terminals in layer 5/6 by pulsed light caused a large short-delay (~19 ms)

590   LFP depolarization that had a smaller amplitude in GE mice when compared to CON mice

591   (144.9 ± 26.97 vs. 67.0 ± 13.80 µV, F(1,23)=3.396, p=0.024) (Fig. 4Ciii, Table 4). Moreover,

592   the firing of prelimbic neurons changed after pulsed light stimulation (Fig. 4D). Analysis of

593   single unit activity (SUA) revealed that a prominent augmentation (311%) of firing rate

594   occurred ~13 ms after the stimulation in 72 out of 239 units (~30.1%) recorded in layer 5/6 of

595   CON mice. In GE mice, only 18 out of 189 units (~9.5%) responded to light stimuli with a

596   weaker (98.4%) and delayed (~22 ms) firing rate increase (Fig. 4D, E). Analysis of

597   modulation index (MI) of the firing rate of all activated units showed that the activated GE

598   neurons fired significantly less when compared to CON (0.796 ± 0.023 vs. 0.615 ± 0.054,

599   F(1,88)= 11.5007, p= 0.001, Fig. 4Eiv). These results indicate that not only hippocampal

600   terminals target fewer prefrontal neurons in GE, but also their efficacy in boosting the firing

601   rate is attenuated.

602   In line with the fewer hippocampal axons targeting prelimbic upper layers (Fig. 1C,

603   4A) even under physiological conditions, their activation with ramp light stimuli led to weak, if

604   any, network effects in both CON (n=13) and GE mice (n=10) (Fig. 5A, Table 4). However,

605   the evoked LFP response had a lower amplitude in GE mice (132.3 ± 27.6 vs. 63.0 ± 17.94

606   µV, F(1,21)=3.939, p=0.047) (Fig. 5B, Table 4). The firing rate and onset of light-induced

607   firing were similar in all investigated mice (Fig. 5C). A smaller fraction of responsive units

608   has been detected in GE (16 out of 18, ~18.8%) when compared to CON (28 out of

609   230,~12.2%) mice (Fig. 5Di-iii). The firing rate MI of all activated units did not differ between

610   CON and GE (0.763 ± 0.029 vs 0.750 ± 0.040, F(1,42)= 0.079, p= 0.780, Fig. 5Div). In line

611   with the data, we propose that the weaker hippocampal innervation of deep prelimbic layers

612   causes poor activation of targeted neurons, whereas similar effects are lacking for neurons

613   in upper layers. However, the strong inter-layer communication amplified within the densely

614   packed upper layers (and possibly "contaminated" by volume conduction) might lead to

615   disrupted network entrainment in both deep and upper layers, as reflected by the smaller

616   amplitude of evoked LFP in GE mice.

617   These results indicate that, especially in layer 5/6, the hippocampal innervation has a

618   weaker power to boost the firing and oscillatory activity in the PL of GE mice.

619 ***Persistent dysfunction of hippocampal drive to prelimbic cortex in pre-juvenile dual-***

620 ***hit GE mice***

621 Since previous studies showed major functional and behavioral deficits as a result of

622 abnormal prefrontal-hippocampal communication in juvenile GE mice (Xu et al., 2019; Chini

623 et al., 2020; Xu et al., 2021), it is likely that this dysfunction persists along with development.

624 To test this hypothesis, we monitored the function of hippocampal innervation of PL in CON

625 and GE mice at pre-juvenile age.

626 First, the function of hippocampal projections in PL was assessed *in vitro*. Similar to

627 the results obtained from coronal slices including the PL from neonatal mice, light stimulation

628 (10 ms, 473 nm) of hippocampal inputs evoked robust excitatory postsynaptic currents in

629 prefrontal neurons from all investigated pre-juvenile mice (Fig. 6A). However, the fraction of

630 responsive neurons was larger in CON (layer 5/6: 67.65%; layer 2/3: 57.14%) when

631 compared to GE mice (layer 5/6: 46.88%; layer 2/3: 31.25%) (Table 3). The light-induced

632 synaptic inputs had faster kinetics when compared to the currents recorded in the neonatal

633 PL in all investigated pre-juvenile mice (Fig. 6Biii-iv, Table 3). The amplitude of the eEPSCs

634 recorded in layer 5/6 was significantly smaller in GE (Fig. 6Bi, 70.1 ± 13.74 vs. 19.7 ± 4.39

635 pA, p=0.0354) and had a higher variability when compared to CON mice (Fig. 6Bii, Table 3).

636 In contrast, the eEPSCs recorded from layer 2/3 neurons were similar in pre-juvenile CON

637 and GE mice. Repetitive stimulation (8 Hz, 10 ms) of hippocampal inputs evoked sustained

638 EPSCs with different response patterns in CON and GE neurons. In contrast to the

639 prominent depression of inputs in all neonatal neurons, a slight depression was detected for

640 layer 2/3 neurons of GE mice, whereas the eEPSCs in layer 5/6 were either facilitated or

641 unchanged (Fig. 6C). However, PPR for layer 2/3 decreased in GE mice and showed a clear

642 depression over higher frequencies. Moreover, there was a significant difference in the value

643 of PPR between CON and GE when light was conducted at 125 ms intervals, but not at 250

644 ms and 500 ms intervals (Fig. 6Dii, Table 3). This means the STP of hippocampal inputs was

645 comparable in response to low frequency stimulation in CON and GE, but differs for high

646 frequency stimulation. Taken together, these results indicate that the dysfunction of

24

647 hippocampal innervation persists at pre-juvenile age in GE mice, yet it appears less

648 pronounced than the deficits reported for neonatal stage.

649   Second, we performed multisite extracellular recordings of LFP and MUA combined

650 with the optogenetic stimulation of hippocampal terminals in pre-juvenile CON (n=17) and

651 GE mice (n=9) *in vivo* (Fig. 6E-H). We used similar stimulation protocols as described for

652 neonatal animals. Ramp light stimulation of hippocampal projections targeting prelimbic

653 layers 5/6 and 2/3 had a minor, if any, effect on the power of network oscillation in CON and

654 GE mice (Table 4). The pulsed light evoked a strong bi-phasic LFP response (Fig. 6Ei, Gi)

655 with comparable amplitude in all investigated mice (Fig. 6Eii, Gii, Table 4). The overall

656 prelimbic firing was augmented upon light stimuli, yet the number of responsive units was

657 lower in layer 5/6 of GE mice (155 out of 342, ~45.3%) when compared to CON mice (221

658 out of 398, ~55.5%) (Fig. 6Fiv). The firing rate MI of all activated units did not differ between

659 CON and GE (0.225 ± 0.023 vs 0.239 ± 0.028, $F_{(1,374)}$= 0.1372, p= 0.712, Fig. 6Fv). When

660 the light activated the hippocampal axonal terminals in layer 2/3, the firing rate strongly

661 augmented in CON but much weaker in GE mice (Fig. 6H). However, the number of

662 activated units was comparable in the two groups of pre-juvenile mice (CON: 121 out of 327,

663 ~38.8%; GE: 86 out of 230 units, ~37.3%) (Fig. 6Hiv). The firing rate MI of all activated units

664 was significant lower in GE when compare to CON (0.178 ± 0.024 vs 0.121 ± 0.013,

665 $F_{(1,206)}$= 3.881, p= 0.049, Fig. 6Hv).

666   Thus, the functional disruption of hippocampal drive to the PL in dual-hit GE mice

667 persists throughout development, although the magnitude and patterns of dysfunction differ

668 from those identified at neonatal age.

669 **Discussion**

670 Many decades ago, disturbed interactions between HP and PFC has been proposed as a

671 core aspect of pathophysiology in psychiatric disorders. Especially in schizophrenia, the

672 prefrontal-hippocampal impairment might link the neurodevelopmental dysfunction and later

673 behavioral deficits (Weinberger, 1987). However, until recently, the experimental evidence

674   for abnormal disease-related prefrontal-hippocampal communication during development

675   was missing. We previously capitalized on *in vivo* recording and manipulation techniques in

676   mouse models of disease and showed that the development of local circuits in both PFC and

677   HP are profoundly impaired when genetic and environmental stressors converge to mimic

678   the psychiatric risk (Xu et al., 2019; Chini et al., 2020; Xu et al., 2021). Moreover, the

679   excitatory drive from the HP to PFC is weaker in these disease models (Hartung et al., 2016;

680   Oberlander et al., 2019). In the present study, we monitor the structure and function of

681   prefrontal-hippocampal connectivity in control and GE mice. We show that in GE mice (i) the

682   sparser axonal projections from HP to PL act as substrate of diminished HP-PFC

683   communication throughout postnatal development; (ii) presynaptic abnormality of

684   hippocampal terminals and their poorer efficiency in activating the PL cause miswiring of

685   long-range connectivity, and (iii) the deficits of hippocampal projections persist, yet at a

686   lower magnitude, until pre-juvenile age.

687   A wealth of studies documented the schizophrenia-characteristic dysconnectivity

688   between HP and PFC in chronic patients, first-episode patients as well as high-risk

689   individuals during cognitive tasks (Meyer-Lindenberg et al., 2005; Benetti et al., 2009; Wolf

690   et al., 2009). The weaker driving force from the HP to PFC has been replicated in different

691   animal models of disease at adult age (Dickerson et al., 2010; Sigurdsson et al., 2010;

692   Mukai et al., 2015). Three possible sources of disconnection have been identified. First, the

693   excitatory drive from the HP is decreased due to cellular dysfunction and altered

694   morphological features of CA1 pyramidal neurons. Post-mortem histology in schizophrenia

695   patients and mouse models as well as monitoring of neuronal and network activity in HP *in*

696   *vivo* and *in vitro* confirmed this hypothesis (Harrison and Weinberger, 2005; Meyer-

697   Lindenberg, 2010; Marissal et al., 2018). Second, abnormal structure and function of both

698   prefrontal pyramidal neurons and interneurons might hamper the normal communication

699   between HP and PFC (Benchenane et al., 2010; Mukai et al., 2015; Sauer et al., 2015;

700   Abbas et al., 2018). Third, decreased connectivity between the two brain areas might serve

701   as a substrate of the decoupling monitored by decreased synchrony between HP and PFC

702   (Meyer-Lindenberg et al., 2005; Cohen, 2011; Mukai et al., 2015).

703   The developmental dysconnectivity between HP and PFC was observed in several

704   animal models of psychiatric disorders that mirror distinct aspects of the disease (Oberlander

705   et al., 2019). In particular, mice that combine the genetic deficits with the action of

706   environmental stressors to mimic the psychiatric risk showed disconnection of PFC and HP

707   towards the end of the first postnatal week (Hartung et al., 2016; Oberlander et al., 2019), a

708   developmental stage that corresponds to the second-third gestational trimester in humans

709   (Clancy et al., 2001). However, in contrast to the previously reported dysfunction in adult

710   mice (Kvajo et al., 2008; Dickerson et al., 2010; Kvajo et al., 2011), DISC1 suppression or

711   MIA alone (single-hit models) had no impact on the neuronal and network function at

712   neonatal age. In dual-hit GE mice, the structure and function of PFC and HP were

713   compromised at neonatal age and the deficits persist, yet sometimes at a lower magnitude,

714   throughout the entire development (Xu et al., 2019; Chini et al., 2020; Xu et al., 2021). These

715   observations support the concept that convergence of genetic and environmental risk factors

716   advances the neuropathology of disease and might cause severer deficits (Uher, 2014). In

717   the present study, we complemented these data and provided experimental evidence for the

718   early prefrontal-hippocampal disconnection.

719   Monitoring of hippocampal projections by different methods revealed the sparser

720   targeting of PFC. The role of DISC1 in dendritic and axonal development is well documented

721   (Morris et al., 2003; Ozeki et al., 2003; Shen et al., 2008; Kvajo et al., 2011). Mutations in

722   Disc1 lead to alterations in neuronal architecture and cognition (Kvajo et al., 2008; Kvajo et

723   al., 2011; Crabtree et al., 2017), that have been reported for schizophrenia, bipolar disorder

724   and major depression (Millar et al., 2000; Blackwood et al., 2001). Given the ability of DISC1

725   to interact with proteins that bind to microtubules and associated complexes, thus regulating

726   cytoskeleton dynamics (Morris et al., 2003; Ozeki et al., 2003; Brandon et al., 2005; Wang

727   and Brandon, 2011), it is not surprising that the long-range axonal projections from HP to

728   PFC are significantly reduced in GE mice. Reduced integrity and anatomical abnormalities in

729   the fornix, the fiber bundle that connects the HP with neocortical areas including the PFC,

730   have been observed in schizophrenia patients. Moreover, hippocampal projections form

731   fewer branches in the PFC of mouse models and has been proposed as an anatomical

732   substrate of prefrontal-hippocampal synchrony deficits (Zhou et al., 2008; Mukai et al., 2015).

733   In line with the structural change, the diminishment of excitatory drive towards PFC neurons

734   was observed. Hippocampal terminals targeted fewer prefrontal neurons in GE mice and

735   their efficacy in boosting the firing of prefrontal neurons was much weaker.

736   Besides the decreased axonal density, multiple presynaptic alterations of

737   hippocampal inputs were found in dual-hit GE mice. The observed AP widening might lead

738   to altered short-term synaptic plasticity by increasing the initial probability of presynaptic

739   release and shifting the presynaptic short-term plasticity toward depression (Abbott and

740   Regehr, 2004). PPR directly relates to presynaptic release probability, yet also re-uptake

741   mechanisms and modulation of neurotransmitter vesicle fusion (Glasgow et al., 2019).

742   Furthermore, our observation that the differences between neonatal CON and GE in short-

743   term depression paradigms were most obvious at lower stimulation frequency (500 ms

744   interval) than at higher stimulus frequency (125 ms interval) supports the impact of wider

745   action potentials in the HP for neurotransmitter release in PFC. It has been shown that the

746   presynaptic characteristics are not fixed throughout development. The depression

747   contributes less to synaptic dynamics, whereas facilitation becomes more prominent (Reyes

748   and Sakmann, 1999; Dittman et al., 2000). At pre-juvenile age, short-term facilitation of

749   hippocampal terminals on prefrontal neurons was observed in CON, supporting the synaptic

750   enhancement during development. However, in GE mice high frequency depression was

751   observed in layer 2/3 neurons of PL. The underlying mechanisms might be presynaptic

752   deregulation of the synaptic vesicle recycling and the release of neurotransmitters (Flores et

753   al., 2011; Tang et al., 2016) or postsynaptic receptor desensitization that make the target

754   neurons less sensitive to neurotransmitter (Zucker and Regehr, 2002). From neonatal to pre-

755   juvenile age, the *in vivo* LFP response to light stimulation of hippocampal terminals was

756   weaker at pre-juvenile age, which might relate to a more mature network balanced by

757   excitation-inhibition. However, the response becomes faster as shown by the shorter onset

758   of eEPSCs and faster firing of prefrontal neurons. These changes are less evident in GE

759   mice. Overall, in addition to the reduced hippocampal innervation and ability in entraining

760   prelimbic activity, alterations in synaptic plasticity reduce the efficiency of these projections.

761   Altogether, these processes may cumulatively impinge on the structure and function of

762   hippocampal-prefrontal network.

763   The results of light stimulation in CON mice provide first insights into the mechanisms

764   of how hippocampal inputs shape the prefrontal excitation-inhibition throughout the

765   development. At neonatal age, few neurons reduced their firing rate after pulsed light

766   stimulation, whereas their number significantly augmented at pre-juvenile age. The

767   decreased firing rates might arise from the feed-forward inhibition of the interneurons that

768   are directly targeted by hippocampal terminals, or from the activation of interneurons directly

769   connected to the light-activated pyramidal neurons. Multiple mechanisms, such as more

770   interneurons are recruited by the hippocampal innervation, the synaptic strength on

771   interneurons increase along with the development, or the interaction between pyramidal

772   neurons and interneurons change with age, might underlie these observations. Our results

773   showed that the depression-to-facilitation shift of hippocampal input on layer 2/3 prelimbic

774   neurons is disrupted in pre-juvenile GE mice. Excitation-inhibition imbalance in PL might

775   underlie numerous neurological and behavioral abnormalities found in GE mice.

776   The present results add experimental evidence for the developmental miswiring of

777   prefrontal-hippocampal networks in psychiatric disorders. The profound dysfunction of these

778   networks already takes place at early stages of development. The sparse and less efficient

779   projections from CA1 area to the PFC do not optimally entrain the prefrontal networks in

780   oscillatory rhythms. Together with the local synaptic deficits in both areas, the weaker

781   connectivity causes an abnormal communication and information processing that, despite

782   partial compensation at pre-juvenile age, might be vulnerable to environmental stressors or

783   age-related changes of neuromodulatory systems (e.g., dopamine) (Arnsten et al., 2012;

784   McEwen and Morrison, 2013; Klune et al., 2021). By these means, the early disconnection

785   between PFC and HP might have a long-lasting impact on memory and executive

786   processing (Hartung et al., 2016; Xu et al., 2019; Chini et al., 2020; Xu et al., 2021). While

787   these data from animal models of disease help to identify possible "hubs" of miswiring early

788   in life, future investigations need to explore the clinical validity of developmental mechanisms

789   of mental disorders.

790   **Author contributions**

791   I.L.H.-O. and L.S. designed the experiments, L.S., X.X., and P.P. performed the experiments

792   and analyzed the data, D.F. and M.S. carried out the Clarity imaging and analysis, I.L.H.-O.

793   and L.S. interpreted the data and wrote the paper. All authors discussed and commented on

794   the manuscript.

795   **References**

796   Abbas AI, Sundiang MJM, Henoch B, Morton MP, Bolkan SS, Park AJ, Harris AZ,

797   Kellendonk C, Gordon JA (2018) Somatostatin Interneurons Facilitate Hippocampal-

798   Prefrontal Synchrony and Prefrontal Spatial Encoding. Neuron 100:926-939 e3.

799   Abbott LF, Regehr WG (2004) Synaptic computation. Nature 431:796-803.

800   Ahlbeck J, Song L, Chini M, Bitzenhofer SH, Hanganu-Opatz IL (2018) Glutamatergic drive

801   along the septo-temporal axis of hippocampus boosts prelimbic oscillations in the

802   neonatal mouse. Elife 7:e33158.

803   Alemany-Gonzalez M, Gener T, Nebot P, Vilademunt M, Dierssen M, Puig MV (2020)

804   Prefrontal-hippocampal functional connectivity encodes recognition memory and is

805   impaired in intellectual disability. PNAS 117:11788-11798.

806   Arnsten AF, Wang MJ, Paspalas CD (2012) Neuromodulation of thought: flexibilities and

807   vulnerabilities in prefrontal cortical network synapses. Neuron 76:223-239.

808   Backus AR, Schoffelen JM, Szebenyi S, Hanslmayr S, Doeller CF (2016) Hippocampal-

809   Prefrontal Theta Oscillations Support Memory Integration. Curr Biol 26:450-457.

810   Bahner F, Meyer-Lindenberg A (2017) Hippocampal-prefrontal connectivity as a translational

811   phenotype for schizophrenia. Eur Neuropsychopharmacol 27:93-106.

812   Benchenane K, Peyrache A, Khamassi M, Tierney PL, Gioanni Y, Battaglia FP, Wiener SI

813   (2010) Coherent theta oscillations and reorganization of spike timing in the

814   hippocampal-prefrontal network upon learning. Neuron 66:921-936.

815   Benetti S, Mechelli A, Picchioni M, Broome M, Williams S, McGuire P (2009) Functional

816   integration between the posterior hippocampus and prefrontal cortex is impaired in

817   both first episode schizophrenia and the at risk mental state. Brain 132:2426-2436.

818   Bitzenhofer SH, Ahlbeck J, Wolff A, Wiegert JS, Gee CE, Oertner TG, Hanganu-Opatz IL

819   (2017) Layer-specific optogenetic activation of pyramidal neurons causes beta-

820   gamma entrainment of neonatal networks. Nat Commun 8:14563.

821   Bora E, Yucel M, Pantelis C (2010) Cognitive impairment in schizophrenia and affective
822   psychoses: implications for DSM-V criteria and beyond. Schizophr Bull 36:36-42.

823   Brandon NJ, Sawa A (2011) Linking neurodevelopmental and synaptic theories of mental
824   illness through DISC1. Nat Rev Neurosci 12:707-722.

825   Brandon NJ, Schurov I, Camargo LM, Handford EJ, Duran-Jimeniz B, Hunt P, Millar JK,
826   Porteous DJ, Shearman MS, Whiting PJ (2005) Subcellular targeting of DISC1 is
827   dependent on a domain independent from the Nudel binding site. Mol Cell Neurosci
828   28:613-624.

829   Blackwood DH, Fordyce A, Walker MT, St Clair DM, Porteous DJ, Muir WJ (2001)
830   Schizophrenia and affective disorders–cosegregation with atranslocation at
831   chromosome 1q42 that directly disrupts brain-expressed genes: Clinical and P300
832   findings in a family. Am J Hum Genet 69:428–433.

833   Brennan GP, Baram TZ, Poolos NP (2016) Hyperpolarization-Activated Cyclic Nucleotide-
834   Gated (HCN) Channels in Epilepsy. Cold Spring Harb Perspect Med 6:a022384.

835   Cenquizca LA, Swanson LW (2007) Spatial organization of direct hippocampal field CA1
836   axonal projections to the rest of the cerebral cortex. Brain Res Rev 56:1-26.

837   Chini M, Popplau JA, Lindemann C, Carol-Perdiguer L, Hnida M, Oberlander V, Xu X,
838   Ahlbeck J, Bitzenhofer SH, Mulert C, Hanganu-Opatz IL (2020) Resolving and
839   Rescuing Developmental Miswiring in a Mouse Model of Cognitive Impairment.
840   Neuron 105:60-74 e7.

841   Chung K, Deisseroth K (2013) CLARITY for mapping the nervous system. Nat Methods
842   10:508-513.

843   Clancy B, Darlington RB, Finlay BL (2001) Translating developmental time across
844   mammalian species. Neuroscience 105:7-17.

845   Cohen MX (2011) Hippocampal-prefrontal connectivity predicts midfrontal oscillations and
846   long-term memory performance. Curr Biol 21:1900-1905.

847   Dere E, Pause BM, Pietrowsky R (2010) Emotion and episodic memory in neuropsychiatric
848   disorders. Behav Brain Res 215:162-171.

849   Diamantopoulou A, Gogos JA (2019) Neurocognitive and Perceptual Processing in Genetic
850   Mouse Models of Schizophrenia: Emerging Lessons. Neuroscientist 25:597-619.

851   Dickerson DD, Wolff AR, Bilkey DK (2010) Abnormal long-range neural synchrony in a
852   maternal immune activation animal model of schizophrenia. J Neurosci 30:12424-
853   12431.

854   Dittman JS, Kreitzer AC, Regehr WG (2000) Interplay between Facilitation, Depression, and
855   Residual Calcium at Three Presynaptic Terminals. The Journal of Neuroscience
856   20:1374-1385.

857   Dolleman-Van Der Weel MJ, Witter MP (1996) Projections from the nucleus reuniens thalami
858   to the entorhinal cortex, hippocampal field CA1, and the subiculum in the rat arise
859   from different populations of neurons. J Comp Neurol 364:637-650.

860   Eichenbaum H (2017) Prefrontal-hippocampal interactions in episodic memory. Nat Rev
861   Neurosci 18:547-558.

862   Flores R, 3rd, Hirota Y, Armstrong B, Sawa A, Tomoda T (2011) DISC1 regulates synaptic
863   vesicle transport via a lithium-sensitive pathway. Neurosci Res 71:71-77.

864   Friston KJ, Frith CD (1995) Schizophrenia: a disconnection syndrome? Clin Neurosci
865   3(2):89-97.

866   Glasgow SD, McPhedrain R, Madranges JF, Kennedy TE, Ruthazer ES (2019) Approaches
867   and Limitations in the Investigation of Synaptic Transmission and Plasticity. Front
868   Synaptic Neurosci 11:20.

869   Greenland-White SE, Ragland JD, Niendam TA, Ferrer E, Carter CS (2017) Episodic
870   memory functions in first episode psychosis and clinical high risk individuals.
871   Schizophr Res 188:151-157.

872   Harrison PJ, Weinberger DR (2005) Schizophrenia genes, gene expression, and
873   neuropathology: on the matter of their convergence. Mol Psychiatry 10:40–68.

874   Hartung H, Cichon N, De Feo V, Riemann S, Schildt S, Lindemann C, Mulert C, Gogos JA,
875   Hanganu-Opatz IL (2016) From Shortage to Surge: A Developmental Switch in

876   Hippocampal-Prefrontal Coupling in a Gene-Environment Model of Neuropsychiatric

877   Disorders. Cereb Cortex 26:4265-4281.

878   Jay TM, Witter MP (1991) Distribution of hippocampal CA1 and subicular efferents in the

879   prefrontal cortex of the rat studied by means of anterograde transport of Phaseolus

880   vulgaris-leucoagglutinin. J Comp Neurol 313:574-586.

881   Jay TM, Glowinski J, Thierry AM (1989) Selectivity of the hippocampal projection to the

882   prelimbic area of the prefrontal cortex in the rat. Brain Res 505:337-340.

883   Kannan G, Sawa A, Pletnikov MV (2013) Mouse models of gene-environment interactions in

884   schizophrenia. Neurobiol Dis 57:5-11.

885   Klune CB, Jin B, DeNardo LA (2021) Linking mPFC circuit maturation to the developmental

886   regulation of emotional memory and cognitive flexibility. Elife 10:e64567.

887   Kvajo M, McKellar H, Arguello PA, Drew LJ, Moore H, MacDermott AB, Karayiorgou M,

888   Gogos JA (2008) A mutation in mouse Disc1 that models a schizophrenia risk allele

889   leads to specific alterations in neuronal architecture and cognition. Proc Natl Acad

890   Sci U S A 105:7076-7081.

891   Kvajo M, McKellar H, Drew LJ, Lepagnol-Bestel AM, Xiao L, Levy RJ, Blazeski R, Arguello

892   PA, Lacefield CO, Mason CA, Simonneau M, O'Donnell JM, MacDermott AB,

893   Karayiorgou M, Gogos JA (2011) Altered axonal targeting and short-term plasticity in

894   the hippocampus of Disc1 mutant mice. PNAS 108:E1349-1358.

895   Liu X, Carter AG (2018) Ventral Hippocampal Inputs Preferentially Drive Corticocortical

896   Neurons in the Infralimbic Prefrontal Cortex. J Neurosci 38:7351-7363.

897   Marissal T, Salazar RF, Bertollini C, Mutel S, De Roo M, Rodriguez I, Muller D, Carleton A

898   (2018) Restoring wild-type-like CA1 network dynamics and behavior during

899   adulthood in a mouse model of schizophrenia. Nat Neurosci 21:1412-1420.

900   McDonald-McGinn DM, Sullivan KE, Marino B, Philip N, Swillen A, Vorstman JA, Zackai EH,

901   Emanuel BS, Vermeesch JR, Morrow BE, Scambler PJ, Bassett AS (2015) 22q11.2

902   deletion syndrome. Nat Rev Dis Primers 1:15071.

903   McEwen BS, Morrison JH (2013) The brain on stress: vulnerability and plasticity of the
904   prefrontal cortex over the life course. Neuron 79:16-29.

905   Meyer-Lindenberg A (2010) From maps to mechanisms through neuroimaging of
906   schizophrenia. Nature 468:194-202.

907   Meyer-Lindenberg AS, Olsen RK, Kohn PD, Brown T, Egan MF, Weinberger DR, Berman
908   KF (2005) Regionally specific disturbance of dorsolateral prefrontal-hippocampal
909   functional connectivity in schizophrenia. Arch Gen Psychiatry 62:379-386.

910   Miller EK, Cohen JD (2001) An integrative theory of prefrontal cortex function. Annu Rev
911   Neurosci 24:167-202.

912   Millar JK, Wilson-Annan JC, Anderson S, Christie S, Taylor MS, Semple CA, Devon RS, St
913   Clair DM, Muir WJ, Blackwood DH, Porteous DJ (2000) Disruption of two novel
914   genes by a translocation co-segregating with schizophrenia. Hum Mol Genet 9:1415-
915   1423.

916   Morris JA, Kandpal G, Ma L, Austin CP (2003) DISC1 (Disrupted-In-Schizophrenia 1) is a
917   centrosome-associated protein that interacts with MAP1A, MIPT3, ATF4/5 and
918   NUDEL: regulation and loss of interaction with mutation. Hum Mol Genet 12:1591-
919   1608.

920   Mukai J, Tamura M, Fenelon K, Rosen AM, Spellman TJ, Kang R, MacDermott AB,
921   Karayiorgou M, Gordon JA, Gogos JA (2015) Molecular substrates of altered axonal
922   growth and brain connectivity in a mouse model of schizophrenia. Neuron 86:680-
923   695.

924   Nestler EJ, Hyman SE (2010) Animal models of neuropsychiatric disorders. Nat Neurosci
925   13:1161-1169.

926   Oberlander VC, Xu X, Chini M, Hanganu-Opatz IL (2019) Developmental dysfunction of
927   prefrontal-hippocampal networks in mouse models of mental illness. Eur J Neurosci
928   50:3072-3084.

929   Owen MJ, Sawa A, Mortensen PB (2016) Schizophrenia. The Lancet 388:86-97.

930   Ozeki Y, Tomoda T, Kleiderlein J, Kamiya A, Bord L, Fujii K, Okawa M, Yamada N, Hatten
931   ME, Snyder SH, Ross CA, Sawa A (2003) Disrupted-in-Schizophrenia-1 (DISC-1):
932   mutant truncation prevents binding to NudE-like (NUDEL) and inhibits neurite
933   outgrowth. PNAS 100:289-294.

934   Padilla-Coreano N, Bolkan SS, Pierce GM, Blackman DR, Hardin WD, Garcia-Garcia AL,
935   Spellman TJ, Gordon JA (2016) Direct Ventral Hippocampal-Prefrontal Input Is
936   Required for Anxiety-Related Neural Activity and Behavior. Neuron 89:857-866.

937   Parent MA, Wang L, Su J, Netoff T, Yuan LL (2010) Identification of the hippocampal input to
938   medial prefrontal cortex in vitro. Cereb Cortex 20:393-403.

939   Pernia-Andrade AJ, Goswami SP, Stickler Y, Frobe U, Schlogl A, Jonas P (2012) A
940   deconvolution-based method with high sensitivity and temporal resolution for
941   detection of spontaneous synaptic currents in vitro and in vivo. Biophys J 103:1429-
942   1439.

943   Phillips ML, Robinson HA, Pozzo-Miller L (2019) Ventral hippocampal projections to the
944   medial prefrontal cortex regulate social memory. Elife 8:e44182.

945   Reyes A, Sakmann B (1999) Developmental switch in the short-term modification of unitary
946   EPSPs evoked in layer 2/3 and layer 5 pyramidal neurons of rat neocortex. J
947   Neurosci 19:3827-3835.

948   Preston AR, Eichenbaum H (2013) Interplay of hippocampus and prefrontal cortex in
949   memory. Curr Biol 23:R764-773.

950   Rossant C, Kadir SN, Goodman DFM, Schulman J, Hunter MLD, Saleem AB, Grosmark A,
951   Belluscio M, Denfield GH, Ecker AS, Tolias AS, Solomon S, Buzsaki G, Carandini M,
952   Harris KD (2016) Spike sorting for large, dense electrode arrays. Nat Neurosci
953   19:634-641.

954   Sauer JF, Struber M, Bartos M (2015) Impaired fast-spiking interneuron function in a genetic
955   mouse model of depression. Elife 4:e04979.

956   Shen S, Lang B, Nakamoto C, Zhang F, Pu J, Kuan SL, Chatzi C, He S, Mackie I, Brandon
957   NJ, Marquis KL, Day M, Hurko O, McCaig CD, Riedel G, St Clair D (2008)

958   Schizophrenia-related neural and behavioral phenotypes in transgenic mice
959   expressing truncated Disc1. J Neurosci 28:10893-10904.

960   Siapas AG, Lubenov EV, Wilson MA (2005) Prefrontal phase locking to hippocampal theta
961   oscillations. Neuron 46:141-151.

962   Sigurdsson T (2016) Neural circuit dysfunction in schizophrenia: Insights from animal models.
963   Neuroscience 321:42-65.

964   Sigurdsson T, Stark KL, Karayiorgou M, Gogos JA, Gordon JA (2010) Impaired
965   hippocampal-prefrontal synchrony in a genetic mouse model of schizophrenia.
966   Nature 464:763-767.

967   Spellman T, Rigotti M, Ahmari SE, Fusi S, Gogos JA, Gordon JA (2015) Hippocampal-
968   prefrontal input supports spatial encoding in working memory. Nature 522:309-314.

969   Stujenske JM, Spellman T, Gordon JA (2015) Modeling the Spatiotemporal Dynamics of
970   Light and Heat Propagation for In Vivo Optogenetics. Cell Rep 12:525-534.

971   Szczurkowska J, Cwetsch AW, dal Maschio M, Ghezzi D, Ratto GM, Cancedda L (2016)
972   Targeted in vivo genetic manipulation of the mouse or rat brain by in utero
973   electroporation with a triple-electrode probe. Nat Protoc 11:399-412.

974   Tang W, Thevathasan JV, Lin Q, Lim KB, Kuroda K, Kaibuchi K, Bilger M, Soong TW, Fivaz
975   M (2016) Stimulation of Synaptic Vesicle Exocytosis by the Mental Disease Gene
976   DISC1 is Mediated by N-Type Voltage-Gated Calcium Channels. Front Synaptic
977   Neurosci 8:15.

978   Uher R (2014) Gene-environment interactions in severe mental illness. Front Psychiatry 5:48.

979   Vertes RP (2006) Interactions among the medial prefrontal cortex, hippocampus and midline
980   thalamus in emotional and cognitive processing in the rat. Neuroscience 142:1-20.

981   Wang Q, Brandon NJ (2011) Regulation of the cytoskeleton by Disrupted-in-schizophrenia 1
982   (DISC1). Mol Cell Neurosci 48:359-364.

983   Weinberger DR (1987) Implications of normal brain development for the pathogenesis of
984   schizophrenia. Arch Gen Psychiatry 44:660-669.

985   Wolf RC, Vasic N, Sambataro F, Hose A, Frasch K, Schmid M, Walter H (2009) Temporally

986   anticorrelated brain networks during working memory performance reveal aberrant

987   prefrontal and hippocampal connectivity in patients with schizophrenia. Prog

988   Neuropsychopharmacol Biol Psychiatry 33:1464-1473.

989   Xu X, Song L, Hanganu-Opatz IL (2021) Knock-Down of Hippocampal DISC1 in Immune-

990   Challenged Mice Impairs the Prefrontal-Hippocampal Coupling and the Cognitive

991   Performance Throughout Development. Cereb Cortex 31:1240-1258.

992   Xu X, Chini M, Bitzenhofer SH, Hanganu-Opatz IL (2019) Transient Knock-Down of

993   Prefrontal DISC1 in Immune-Challenged Mice Causes Abnormal Long-Range

994   Coupling and Cognitive Dysfunction throughout Development. J Neurosci 39:1222-

995   1235.

996   Zhou Y, Shu N, Liu Y, Song M, Hao Y, Liu H, Yu C, Liu Z, Jiang T (2008) Altered resting-

997   state functional connectivity and anatomical connectivity of hippocampus in

998   schizophrenia. Schizophr Res 100:120-132.

999   Zucker RS, Regehr WG (2002) Short-term synaptic plasticity. Annu Rev Physiol 64:355-405.

1000

1001   **Legends**

1002   **Figure 1. Organization and developmental dynamics of hippocampal innervation of PL**

1003   **in neonatal and pre-juvenile dual-hit GE mice**. **A**, Schematic representation of tracing

1004   protocols. Mice were injected unilaterally with the retrograde tracer FG into PL or with either

1005   the anterograde tracer BDA or the transsynaptic tracer WGA into HP. **B**, Left, fluorescent

1006   images of FG (white) injection site in the PL of 50 μm-thick coronal slice from a P10 mouse

1007   when co-stained with NeuN (green). Right, corresponding NeuN-stained coronal slices (50

1008   μm-thick) including the dorsal HP (dHP), intermediate HP (iHP), and ventral HP (vHP) with

1009   retrogradely stained cells (white). Scale bar, 500 μm. Insets, FG-stained neurons (white)

1010   shown at higher magnification. Scale bar, 100 μm. **C**, Photograph of a representative BDA

1011   injection into the i/vHP of a P10 mouse visualized by streptavidin staining (green) and co-

1012   stained with DAPI (blue) in a 50 μm-thick coronal slice. **D**, 3D reconstruction of hippocampal

1013   axons (tDimer, red) into the PL (cyan surface) in a cleared P10 mouse brain. PL volume was

1014   delimited according to nuclei staining (DRAQ5; not shown). Inset, logarithmic violin plots

1015   depicting the relative space occupancy of hippocampal fibers within PL, normalized to the

1016   number of transfected neurons in i/vHP. **E**, Left, orthogonal views of the Z-stack (YZ, XZ)

1017   images illustrating BDA-positive boutons (green) that colocalized with vGLUT1 (red). Right,

1018   confocal images displaying BDA-positive boutons (green) on GABA-positive (red) somata

1019   (arrows) and GABA-negative neurons (asterisk). **F**, Left, a representative example of WGA

1020   staining (magenta) in a 50 μm-thick coronal slice including the PFC of a P10 mouse that

1021   transsynaptically labeled neurons targeted by hippocampal axons. Dotted lines mark the

1022   borders of the two subdivisions as well the prelimbic layers. Right, photographs displaying

1023   the colocalization of WGA (magenta) and GABA (cyan) staining for GABA-positive neurons

1024   (circle). GABA-negative but WGA-positive neurons are marked by squares. **G**, (i),

1025   Photograph of BDA-labeled hippocampal terminals (black) targeting deep layers of PL from

1026   a P10 CON (left) and a P10 GE (right) mouse, respectively. **(ii)**, Schematic illustrating the

1027   extent of the BDA injections into the i/vHP of neonatal CON (gray) and dual-hit GE (green)

1028   mice. **(iii)**, Violin plots of the normalized density of hippocampal terminals (in μm/mm2/cell)

1029   in layer 2/3 and layer 5/6 of PL averaged for all investigated neonatal CON and GE mice. **H**,

1030   Same as **G**, for pre-juvenile mice. **I**, Photograph of FG-labeled neurons (white) in the CA1

1031   area of i/vHP in a 50 µm-thick NeuN-stained (green) coronal slice from a P10 CON and a

1032   P10 GE mouse, respectively. **J**, Violin plots of the normalized density of PL-projecting

1033   neurons in the hippocampal CA1 area averaged for all investigated neonatal (left) and pre-

1034   juvenile (right) CON and GE mice. PL: prelimbic cortex, IL: infralimbic cortex, Cg: cingulate

1035   cortex, SO: stratum oriens, SP: stratum pyramidale, SR: stratum radiatum. Single data

1036   points are represented as dots and the red horizontal bars in violin plots correspond to the

1037   median and the 25th and 75th percentiles. *p < 0.05.

1038   **Figure 2. Passive and active membrane properties as well as synaptic inputs of**

1039   **prelimbic and hippocampal neurons from neonatal and pre-juvenile CON and GE mice**

1040   ***in vitro***. **A**, Confocal image showing a biocytin-filled pyramidal neuron in layer 5/6 of PL from

1041   a P10 CON mouse. **B**, Representative voltage responses to the injection of hyper- and

1042   depolarizing current pulses (holding membrane potential of -70 mV) of pyramidal neurons in

1043   layer 5/6 (light gray), layer 2/3 (dark gray) of the PL from P10 CON mice as well as for

1044   pyramidal neurons in layer 5/6 (light green), layer 2/3 (dark green) of the PL from P10 GE

1045   mice. **C**, Firing rate in relationship to current injection displayed for layer 5/6 (n=33) and layer

1046   2/3 (n=25) neurons from neonatal CON mice as well as for layer 5/6 (n=20) and layer 2/3

1047   (n=14) from neonatal GE mice. * indicates the comparison of firing rate of layer 2/3 neurons

1048   in response to 120 pA current injection between CON and GE. **D**, Same as **C**, for pre-

1049   juvenile mice (n=28 for CON layer 5/6, n=15 for CON layer 2/3, n=20 for GE layer 5/6, n=12

1050   for GE layer 2/3). **E**, **(i)**, Representative traces of sEPSCs recorded from layer 2/3 pyramidal

1051   neurons from P10 CON (gray) and GE (green) mice. **(ii)**, Cumulative probability distribution

1052   of inter-event intervals (IEIs) and violin plots (inset) of sEPSCs frequencies averaged for all

1053   prefrontal neurons in CON and GE mice. **(iii)**, Same as **(ii)** for sEPSC amplitude. **F**, Same as

1054   **E**, for pre-juvenile mice. **G**, Confocal image showing a biocytin-filled pyramidal neuron in the

1055   CA1 area of i/vHP from a P10 CON mouse. SO: stratum oriens, SP: stratum pyramidale, SR:

1056   stratum radiatum. **H**, Representative voltage responses to the injection of hyper- and

1057   depolarizing current pulses (holding membrane potential of -70 mV) of CA1 pyramidal

1058   neurons from P10 CON (black) and GE (green) mice. **I**, Firing rate in relationship to current

1059   injection displayed for CA1 neurons from neonatal CON (n=15, black) and GE (n=10, green)

1060   mice. **J**, Same as **I**, for pre-juvenile CA1 neurons (n=12 for CON, n=9 for GE). Single data

1061   points are represented as dots and the red horizontal bars in violin plots correspond to the

1062   median and the 25th and 75th percentiles. $*p < 0.05$, $**p < 0.01$.

1063   **Figure 3. Synaptic properties and plasticity of hippocampal inputs on prelimbic**

1064   **pyramidal neurons in neonatal CON and GE mice. A**, **(i)**, Representative image showing

1065   ChR2 (H134R) (red) expression in a DAPI-stained coronal slice from a P10 CON mouse

1066   following hippocampal injection at P1. **(ii)**, Schematic of light stimulation of hippocampal CA1

1067   neurons expressing ChR2 (H134R) (red). **(iii)**, Voltage responses of a ChR2-expressing

1068   neuron to light stimuli (470 nm, 5-10 mW/mm^2) of 2-500 ms duration. **B**, **(i)**, Representative

1069   image showing hippocampal axons (red) in PL and IL from a P10 CON mouse following

1070   hippocampal injection at P1. **(ii)**, Schematic of light stimulation of hippocampal axons in PL.

1071   **(iii)**, Violin plots of eEPSC amplitudes evoked by light stimuli of 3, 5, 10 ms duration. Data

1072   were collected from layer 5/6 pyramidal neurons (n=24) in PL of CON mice. **C**, **(i)**, Left,

1073   representative current responses to light stimulation (blue bar 10 ms) of HP terminals for a

1074   putative pyramidal neuron (red, holding potential of -70 mV; gray, -40 mV, black, 10 mV).

1075   The response was abolished by bath CNQX (blue trace). Right, representative voltage

1076   response to light stimulation (blue bar 10 ms) of HP terminals for a pyramidal neuron. **(ii)**,

1077   Same as **Ci** for a putative interneuron. **D**, Average eEPSC (holding potential of -70mV)

1078   evoked by light in layer 5/6 (n=24) and layer 2/3 (n=21) neurons from neonatal CON mice as

1079   well as for pyramidal neurons in layer 5/6 (n=10) and layer 2/3 (n=8) from neonatal GE mice.

1080   Blue bar corresponds to 10 ms light stimulation. Inset, bar diagram of the percentage of

1081   responsive pyramidal neurons in different groups. **E**, Violin plots showing the **(i)** amplitudes,

1082   **(ii)** coefficient of variation of amplitudes, **(iii)** synaptic delay and **(iv)** rise tau of eEPSCs

1083   averaged for all prefrontal neurons in CON and GE mice. **F**, **(i)**, Representative current

1084   response to pulsed light (8 Hz) (blue) of a layer 5/6 pyramidal neuron from a P10 CON

1085   mouse. **(ii)**, Plot of eEPSC amplitude (normalized to the 1st EPSC amplitude) in response to

1086   8 Hz stimulation averaged for all prefrontal neurons in CON and GE mice. **G**, **(i)**,

1087   Representative response to light stimuli (500 ms inter-stimulus interval) of a layer 5/6

1088   pyramidal neuron from a P10 CON mouse. **(ii)**, Plot of PPR at 125, 250, 500 ms inter-

1089   stimulus intervals averaged for all prefrontal neurons in CON and GE mice. Single data

1090   points are represented as dots and the red horizontal bars in violin plots correspond to the

1091   median and the 25th and 75th percentiles. $*p < 0.05$, $**p < 0.01$.

1092   **Figure 4. Oscillatory activity and neuronal firing in prelimbic layer 5/6 after**

1093   **optogenetic activation of hippocampal terminals in neonatal CON and GE mice *in vivo.***

1094   **A**, Digital photomontage reconstructing the location of a 4-shank recording electrode in a

1095   DAPI-stained 100 μm-thick coronal section (blue) with hippocampal terminals expressing

1096   ChR2 (H134R) (red) from a P9 mouse. Inset, the position of recording sites (white) over the

1097   prelimbic layers displayed at higher magnification. Blue lines correspond to the iso-contour

1098   lines of light intensity (diameter 50 μm, numerical aperture 0.22, light parameters: 473 nm, 2

1099   mW) for 5 and 10 mW/mm^2. **B**, **(i)**, Schematic of ramp light stimulation of hippocampal

1100   terminals in layer 5/6 of PL. **(ii)**, Power of oscillatory activity in layer 5/6 during ramp

1101   stimulation of hippocampal terminals in layer 5/6, normalized to the activity 1.5 s before

1102   stimulation in CON (gray) and GE (green) mice. **(iii)**, Violin plots displaying the oscillatory

1103   power averaged for different frequency bands (4–12 Hz, 12–30 Hz, 30–50 Hz) in response

1104   to ramp stimulation for all investigated CON and GE mice. **C**, **(i)**, Schematic of pulses light

1105   stimulation of hippocampal terminals in layer 5/6 of PL. **(ii)**, Averaged LFP traces recorded in

1106   layer 5/6 in response to light stimulation of HP terminals (blue bars) in CON (gray) and GE

1107   (green) mice. **(iii)**, Violin plots showing the average amplitude of the maximum LFP

1108   response in layers 5/6 of CON and GE mice. **(iv)**, Violin plots showing the average delay of

1109   the maximum LFP response in layers 5/6 of CON and GE mice. **D**, **(i)**, Raster plot depicting

1110   the firing of single prelimbic cells in response to the pulse stimulation of hippocampal

1111   terminals in layer 5/6 of CON mice. **(ii)**, Same as **(i)**, for GE mice. **(iii)**, Firing rate of all units

1112   in layer 5/6 around the pulse stimulation averaged for CON (gray) and GE (green) mice. **E**,

1113   **(i)**, Modulation index of spiking response of prefrontal single units to pulse stimulation in

1114   layer 5/6 of CON mice. Modulation index > 0 indicates increased firing activity, whereas

1115   values < 0 correspond to decreased firing activity. **(ii)**, Same as **(i)**, for GE mice. **(iii)**,

1116   Stacked bar plot showing the percentage of activated (red), unmodulated (white), and

1117   inhibited (blue) units after the pulse stimulation in layers 5/6 of CON and GE. **(iv)**, Violin plots

1118   showing the modulation index of firing rate of all activated units in layers 5/6 of CON and GE.

1119   Single data points are represented as dots and the red horizontal bars in violin plots

1120   correspond to the median and the 25th and 75th percentiles. *p < 0.05.

1121   **Figure 5. Oscillatory activity and neuronal firing in prelimbic layer 2/3 after**

1122   **optogenetic activation of hippocampal terminals in neonatal CON and GE mice *in vivo*.**

1123   **A**, **(i)**, Schematic of ramp light stimulation of hippocampal axonal terminals in layer 2/3 of PL.

1124   **(ii)**, Power of oscillatory activity in PL layer 2/3 during ramp stimulation of hippocampal

1125   terminals in layer 2/3, normalized to the activity 1.5 s before stimulation in CON (gray) and

1126   GE (green) mice. **(iii)**, Violin plots displaying the oscillatory power averaged for different

1127   frequency bands (4–12 Hz, 12–30 Hz, 30–50 Hz) in response to ramp stimulation for all

1128   investigated CON and GE mice. **B**, **(i)**, Schematic of pulses light stimulation of hippocampal

1129   terminals in layer 2/3 of PL. **(ii)**, Averaged LFP response recorded in prelimbic layer 2/3 in

1130   response to light stimulation (blue bars) of HP terminals in CON (gray) and GE (green) mice.

1131   **(iii)**, Violin plots showing the average amplitude of the maximum LFP response evoked by

1132   light in layers 2/3 of CON and GE. **(iv)**, Violin plots showing the average delay of the

1133   maximum LFP response evoked by light in layers 2/3 of CON and GE. **C**, **(i)**, Raster plot

1134   depicting the firing of single prelimbic cells in response to the pulse stimulation of

1135   hippocampal terminals in layer 2/3 of CON mice. **(ii)**, Same as **(i)**, for GE mice. **(iii)**, Firing

1136   rate of all units in layer 2/3 around the pulse stimulation averaged for CON (gray) and GE

1137   (green) mice. **D**, **(i)**, Modulation index of spiking response of prefrontal single units to pulse

1138   stimulation in layer 2/3 of CON mice. Modulation index > 0 indicates increased firing activity,

1139   whereas values < 0 correspond to decreased firing activity. **(ii)**, Same as **(i)**, for GE mice.

1140   **(iii)**, Stacked bar plot showing the percentage of activated (red), unmodulated (white), and

1141   inhibited (blue) units after the pulse stimulation in layers 2/3 of CON and GE. **(iv)**, Violin plots

1142   showing the modulation index of firing rate of all activated units in layers 2/3 of CON and GE.

1143   Single data points are represented as dots and the red horizontal bars in violin plots

1144   correspond to the median and the 25th and 75th percentiles. *$p < 0.05$.

1145   **Figure 6. Responses of PL during optogenetic activation of hippocampal terminals in**

1146   **pre-juvenile CON and GE mice *in vitro* and *in vivo*. A**, Averaged eEPSC (holding

1147   potential of -70mV) evoked by light in layer 5/6 (n=23) and layer 2/3 (n=15) neurons from

1148   pre-juvenile CON mice as well as in pyramidal neurons in layer 5/6 (n=12) and layer 2/3 (n=6)

1149   from pre-juvenile GE mice. Blue bar corresponds to 10 ms light stimulation. Inset, bar

1150   diagram of the percentage of responsive pyramidal neurons in different groups. **B**, Violin

1151   plots showing the **(i)** amplitudes, **(ii)** coefficient of variation of amplitudes, **(iii)** synaptic delay,

1152   and **(iv)** rise tau of eEPSCs averaged for all prefrontal neurons in CON and GE mice. **C**, **(i)**,

1153   Representative current response to pulsed light (8 Hz) (blue) of a layer 5/6 pyramidal neuron

1154   from a P21 CON mouse. **(ii)**, Plot of eEPSC amplitude (normalized to the 1st EPSC

1155   amplitude) in response to 8 Hz stimulation averaged for all prefrontal neurons in CON and

1156   GE mice. **D**, **(i)**, Representative response to light stimuli (500 ms inter-stimulus interval) of a

1157   layer 5/6 pyramidal neuron from a P21 CON mouse. **(ii)**, Plot of PPR at 125, 250, 500 ms

1158   inter-stimulus intervals averaged for all prefrontal neurons in CON and GE mice. * for

1159   comparison of layer 5/6, ## for comparison of layer 2/3. **E**, **(i)**, Averaged LFP response

1160   recorded in prelimbic layer 5/6 in response to light stimulation (blue bars) of HP terminals in

1161   CON (gray) and GE (green) mice. **(ii)**, Violin plots showing the average amplitude of the

1162   maximum LFP response evoked by light in layer 5/6 of CON and GE mice. **F**, **(i)**, Raster plot

1163   depicting the firing of single prelimbic cells in response to pulse stimulation of hippocampal

terminals in layer 5/6 of CON mice. **(ii)**, Same as **(i)**, for GE mice. **(iii)**, Firing rate of all units

in layer 5/6 around the pulse stimulation averaged for CON (gray) and GE (green) mice. **(iv)**,

Stacked bar plot showing the percentage of activated (red), unmodulated (white), and

inhibited (blue) units after pulse stimulation of prelimbic layer 5/6 of CON and GE mice. **(v)**,

Violin plots showing the modulation index of firing rate of all activated units in layer 5/6 of

CON and GE mice. **G**, Same as in **E**, but for the stimulation in layer 2/3 of PL. **H**, Same as in

F, but for spike response of single prefrontal cells to pulse stimulation of hippocampal

terminals in layer 2/3. Single data points are represented as dots and the red horizontal bars

in violin plots correspond to the median and the 25th and 75th percentiles. *$p < 0.05$, **$p <$

0.01.

Table 1. Passive and active membrane properties of prefrontal and hippocampal

neurons from neonatal and pre-juvenile CON and GE mice *in vitro*. Data are shown as

mean ± SEM. Significance was assessed using one-way analysis of variance (ANOVA) test

followed by Bonferroni-corrected post hoc test and the listed p values correspond to

comparisons between CON and GE mice for the neurons in the same region.

Table 2. Properties of sEPSCs recorded from prefrontal neurons in CON and GE mice

***in vitro*.** Data are shown as mean ± SEM. Significance was assessed using two-way

analysis of variance (ANOVA) test followed by Bonferroni-corrected post hoc test. The listed

p values (*) correspond to comparisons CON L5/6 vs. GE L5/6 and CON L2/3 vs. GE L2/3,

whereas p values (###) correspond to comparisons CON L5/6 vs. CON L2/3, GE L5/6 vs.GE

L2/3.

Table 3. Properties of EPSCs evoked by stimulation of hippocampal terminals *in vitro*.

Data are shown as mean ± SEM. Significance was assessed using one-way analysis of

variance (ANOVA) test followed by Bonferroni-corrected post hoc test. The listed p values

(*$p < 0.05$, **$p < 0.01$) correspond to comparisons CON L5/6 vs. GE L5/6 and CON L2/3 vs.

GE L2/3, whereas p values (##$p < 0.01$) correspond to comparisons CON L5/6 vs. CON L2/3

and GE L5/6 vs. GE L2/3.

1191 **Table 4. Prefrontal activity patterns induced by light stimulation of hippocampal**

1192 **terminals at neonatal and pre-juvenile age.** Data are shown as mean ± SEM. Significance

1193 was assessed using one-way ANOVA test followed by Bonferroni-corrected post hoc test.

1194 The listed P values correspond to comparisons CON L5/6 vs. GE L5/6 and CON L2/3 vs. GE

1195 L2/3.

1196 **Multimedia and 3D Models**

1197 **Multimedia 1: Hippocampal projections to the prelimbic cortex**

1198 3D reconstruction of traced hippocampal terminals in PL from a neonatal CON mouse after

1199 tissue clearing. tDimer expression (red), nuclei staining (cyan). The PL (cyan surface) was

1200 outlined according to nuclei staining. tDimer labeled fibers were segmented and the signal

1201 was enhanced.

1202

1203   **Table 1. Passive and active membrane properties of prefrontal and hippocampal neurons from neonatal and pre-juvenile CON and GE mice *in vitro*.**

		Membrane Properties	Layer 5/6			Layer 2/3			HP		
			CON	GE	p	CON	GE	p	CON	GE	p
Neonatal (P8-P10)	Passive	R_{in} (MΩ)	401.8 ± 19.5	427.6 ± 35.1	0.5352	471.3 ± 18	536.1 ± 35.8	0.0699	453.8 ± 19.8	361.3 ± 16.1	**0.0008**
		C_m (pF)	125.1 ± 5.6	125.6 ± 13.9	0.9693	94.2 ± 4.4	90.5 ± 3.3	0.5804	118.1 ± 5.8	109.7 ± 5.52	0.2559
		τ_m (ms)	83.9 ± 4.3	81.4 ± 8.0	0.7876	67.2 ± 3.5	73.4 ± 4.6	0.2879	49.6 ± 2.6	41.4 ± 2.9	**0.0376**
		RMP (mV)	-68.4 ± 0.7	-67.2 ± 0.9	0.3986	-69.8 ± 0.9	-65.8 ± 1.1	**0.0096**	-69.2 ± 0.8	-69.0 ± 0.7	0.3016
		Sag (%)	10.2 ± 0.9	12.8 ± 2.5	0.2225	4.4 ± 0.62	4.58 ± 0.38	0.8457	23.7 ± 1.2	29.3 ± 1.2	**0.0028**
	Active	AP threshold (mV)	-42.4 ± 1.3	-42.8 ± 2.1	0.9080	-38.8 ± 1.2	-39.1 ± 1.3	0.8544	-40.5 ± 1.0	-43.0 ± 1.3	0.1148
		AP amplitude (mV)	71.5 ± 1.3	69.4 ± 2.2	0.8525	66.8 ± 1.4	59.5 ± 1.8	**0.0028**	80.7 ± 1.4	81.9 ± 1.4	0.5591
		AP halfwidth (ms)	3.56 ± 0.15	3.40 ± 0.18	0.5970	2.85 ± 0.06	3.38 ± 0.15	**0.00062**	2.05 ± 0.04	2.25 ± 0.07	**0.0085**
		Rheobase (pA)	43.5 ± 3.6	40.4 ± 45.0	0.6716	43.1 ± 2.9	46.6 ± 6.8	0.5710	58.3 ± 2.7	59.3 ± 2.6	0.7863
		Firing rate (Hz)	12.3 ± 0.7	11.3 ± 1.1	0.4956	12.5 ± 1.0	11.3 ± 1.6	0.4945	12.5 ± 0.7	12.3 ± 0.8	0.7438
Pre-juvenile (P20-P24)	Passive	R_{in} (MΩ)	222.2 ± 11.5	188.9 ± 17.9	0.1146	235.4 ± 13.2	237.8 ± 9.7	0.8938	239.0 ± 19.6	211.9 ± 24.7	0.3703
		C_m (pF)	178.2 ± 12.5	184.7 ± 13.9	0.7547	131.3 ± 9.37	115.2 ± 8.4	0.2409	174.9 ± 24.0	131.9 ± 22.8	0.1997
		τ_m (ms)	59.6 ± 5.8	45.9 ± 4.7	0.1353	46.9 ± 3.64	44.5 ± 2.9	0.6337	37.7 ± 1.6	33.2 ± 5.1	0.3286
		RMP (mV)	-69.5 ± 0.5	-69.3 ± 0.5	0.8084	-66.9 ± 0.5	-69.7 ± 0.4	**0.00076**	-64.9 ± 1.1	-63.5 ± 2.0	0.5000
		Sag (%)	16.2 ± 1.7	18.4 ± 2.7	0.4839	6.4 ± 1.6	4.3 ± 0.7	0.3337	27.3 ± 2.0	21.1 ± 2.8	0.0664
	Active	AP threshold (mV)	-46.1 ± 1.3	-48.4 ± 2.0	0.3297	-44.5 ± 1.2	-46.4 ± 1.7	0.3370	-45.4 ± 1.8	-49.3 ± 1.9	0.1325
		AP amplitude (mV)	90.1 ± 1.1	90.9 ± 1.6	0.6539	88.5 ± 1.1	86.8 ± 1.3	0.3388	97.1 ± 2.7	96.8 ± 4.4	0.9528
		AP halfwidth (ms)	1.67 ± 0.05	1.53 ± 0.07	0.6839	1.79 ± 0.06	1.65 ± 0.07	0.1186	1.73 ± 0.04	1.74 ± 0.06	0.8715
		Rheobase (pA)	73.8 ± 5.2	78.6 ± 9.3	0.6231	85.1 ± 6.2	89.5 ± 7.8	0.6694	50.7 ± 2.7	48.4 ± 5.1	0.6444
		Firing rate (Hz)	11.4 ± 0.8	10.2 ± 1.3	0.4260	11.8 ± 0.7	10.6 ± 1.1	0.3109	15.0 ± 1.2	15.9 ± 1.8	0.7774

1204
1205   Data are shown as mean ± SEM. Significance was assessed using one-way analysis of variance (ANOVA) test followed by Bonferroni-corrected post hoc test and the listed p
1206   values correspond to comparisons between CON and GE mice for the neurons in the same region.

1207   **Table 2. Properties of sEPSCs recorded from prefrontal neurons in CON and GE mice *in vitro*.**

sEPSC properties		L5/6		L2/3		F values CON vs. GE	F values L5/6 vs. L2/3	F values interaction
		CON	GE	CON	GE			
Neonatal (P8-P10)	Frequency (Hz)	0.24 ± 0.023 ### $p< 0.0001$	0.19 ± 0.022	0.45 ± 0.037 *$p=0.040$	0.31 ± 0.041	$F(1, 92) = 8.141$ $P = 0.005$	$F(1, 92) = 26.43$ $P < 0.0001$	$F(1, 92) = 1.844$ $P = 0.178$
	Amplitude (pA)	7.40 ± 0.22	7.45 ± 0.36	6.92 ± 0.36	7.75 ± 0.56	$F(1, 92) = 2.08$ $P = 0.153$	$F(1, 92) = 0.08$ $P = 0.773$	$F(1, 92) = 1.645$ $P = 0.203$
Pre-juvenile (P20-P24)	Frequency (Hz)	0.93 ± 0.074	0.79 ± 0.083 *$p=0.018$	1.28 ± 0.15	1.41 ± 0.18	$F(1, 101) = 0.002$ $P = 0.967$	$F(1, 101) = 14.44$ $P = 0.0002$	$F(1, 101) = 1.200$ $P = 0.276$
	Amplitude (pA)	7.97 ± 0.27	7.88 ± 0.42	7.45 ± 0.47	7.09 ± 0.53	$F(1, 101) = 0.227$ $P = 0.635$	$F(1, 101) = 1.896$ $P = 0.172$	$F(1, 101) = 0.077$ $P = 0.782$

1208
1209 Data are shown as mean ± SEM. Significance was assessed using two-way analysis of variance (ANOVA) test followed by Bonferroni-corrected post hoc test. The listed p
1210 values (*) correspond to comparisons CON L5/6 vs. GE L5/6 and CON L2/3 vs. GE L2/3, whereas p values (###) correspond to comparisons CON L5/6 vs. CON L2/3, GE L5/6
1211 vs. GE L2/3.

1212   **Table 3. Properties of EPSCs evoked by stimulation of hippocampal terminals *in vitro*.**

Light-evoked EPSCs	Neonatal					Pre-juvenile				
	CON L5/6	GE L5/6	CON L2/3	GE L2/3	F values	CON L5/6	GE L5/6	CON L2/3	GE L2/3	F values
Response %	24/29 (82.76%)	10/24 (41.67%)	21/26 (80.76%)	8/18 (44.44%)		23/34 (67.65%)	15/32 (46.88%)	12/21 (57.14%)	6/16 (37.5%)	
Amplitude (pA)	63.6 ± 12.12 **p=0.001	9.72 ± 2.41	47.9 ± 12.00	40.97 ± 13.6	$F_{(3, 59)}$=14.02 P=0.0029	70.1 ± 13.74 *p=0.0354	19.7 ± 4.39	43.0 ± 14.32	26.2 ± 15.96	$F_{(3, 52)}$=9.877 P=0.0196
Coefficient of variation	0.236 ± 0.032 *p=0.016	0.421 ± 0.052	0.390 ± 0.04	0.416 ± 0.066	$F_{(3, 59)}$=5.35 P=0.0026	0.34 ± 0.041 **p= 0.0005	0.60 ± 0.037	0.45 ± 0.063	0.40 ± 0.049	$F_{(3, 52)}$=6.045 P=0.0012
Onset delay (ms)	5.15 ± 0.476 **p=0.006	7.99 ± 0.762	6.29 ± 0.382	7.55 ± 1.128	$F_{(3, 59)}$=5.00 P=0.0037	4.41 ± 0.508	3.75 ± 0.506 ##p= 0.0044	4.89 ± 0.378	5.15 ± 0.861	$F_{(3, 52)}$=5.967 P=0.0014
Tau rise (ms)	3.07 ± 0.044 *p= 0.022	3.60 ± 0.301	3.18 ± 0.093	3.06 ± 0.171	$F_{(3, 59)}$=3.20 P=0.030	3.63 ± 0.212	3.20 ± 0.158	3.31 ± 0.183	3.11 ± 0.159	$F_{(3, 52)}$=1.358 P=0.2651
PPR 125 ms	0.70 ± 0.056	0.48 ± 0.15	0.64± 0.09	0.63 ± 0.13	$F_{(3, 59)}$=2.28 P=0.5156	1.23 ± 0.09 *p=0.037	0.94 ± 0.13	0.96 ± 0.12 *p= 0.0086	0.51 ± 0.12	$F_{(3, 52)}$=17.11 P=6.70E-04
PPR 250 ms	0.72 ± 0.06	0.54 ± 0.08	0.69± 0.06	0.68 ± 0.15	$F_{(3, 59)}$=3.95 P=0.2672	1.35 ± 0.08	1.19 ± 0.14	1.07 ± 0.15	0.87 ± 0.14	$F_{(3, 52)}$=8.88 P=0.0310
PPR 500 ms	0.66 ± 0.056 **p=0.0061	0.27 ± 0.104	0.70± 0.069	0.62± 0.079	$F_{(3, 59)}$=11.09 P=0.0074	1.28 ± 0.111	1.23 ± 0.108	0.98 ± 0.105	1.03 ± 0.174	$F_{(3, 52)}$=5.505 P=0.1384

1213
1214   Data are shown as mean ± SEM. Significance was assessed using one-way analysis of variance (ANOVA) test followed by Bonferroni-corrected post hoc test. The listed p
1215   values (*p< 0.05, **p< 0.01) correspond to comparisons CON L5/6 vs. GE L5/6 and CON L2/3 vs. GE L2/3, whereas p values (##p< 0.01) correspond to comparisons CON L5/6
1216   vs. CON L2/3, GE L5/6 vs. GE L2/3.

Early misconnectivity in a psychiatric risk model   Song et al.

1217   **Table 4. Prefrontal activity patterns induced by light stimulation of hippocampal terminals at neonatal and pre-juvenile age.**

			Neonatal			Pre-juvenile		
			CON L5/6	GE L5/6	F values	CON L5/6	GE L5/6	F values
Layer 5/6 stimulation	Power (Stim-pre)/pre	4-12 Hz	0.807 ± 0.121	0.218 ± 0.096	F(1,23)=3.365 P=0.039	0.071 ± 0.036	-0.02 ± 0.034	F(1,26)=1.716 P=0.190
		12-30 Hz	0.701 ± 0.141	0.216 ± 0.0562	F(1,23)=1.779 P=0.182	0.056 ± 0.027	0.042 ± 0.019	F(1,26)=0.114 P=0.735
		30-45 Hz	0.383 ± 0.062	0.151 ± 0.061	F(1,23)=2.913 P=0.0846	0.063 ± 0.043	0.079 ± 0.023	F(1,26)=0.179 P=0.673
	evoked LFP	Amplitude (µV)	144.9 ± 26.97	67.0 ± 13.80	F(1,23)=3.396 P=0.024	70.8 ± 7.88	63.1 ± 3.43	F(1,26)=0.007 P=0.936
		Delay (ms)	19.3 ± 0.40	19.3 ± 0.89	F(1,23)=0.365 P=0.552	17.5 ± 0.41	17.1 ± 0.57	F(1,26)=0.392 P=0.537
Layer 2/3 stimulation	Power (Stim-pre)/pre	4-12 Hz	0.289 ± 0.109	0.106 ± 0.135	F(1,21)=2.314 P=0.128	0.052 ± 0.029	0.0003 ± 0.031	F(1,26)=1.517 P=0.218
		12-30 Hz	0.285 ± 0.103	0.272 ± 0.142	F(1,21)=0.314 P=0.575	0.028 ± 0.028	0.036 ± 0.021	F(1,26)=0.070 P=0.792
		30-45 Hz	0.231 ± 0.074	0.098 ± 0.066	F(1,21)=2.827 P=0.093	0.044 ± 0.031	0.036 ± 0.030	F(1,26)=0.008 P=0.930
	evoked LFP	Amplitude (µV)	132.3 ± 27.6	63.0 ± 17.94	F(1,21)=3.939 P=0.047	58.9 ± 8.20	39.7 ± 4.83	F(1,26)=3.282 P=0.07
		Delay (ms)	19.8 ± 0.48	20.2 ± 0.68	F(1,21)=0.013 P=0.910	17.6 ± 0.32	17.2 ± 0.52	F(1,26)=0.910 P=0.350

1218
1219   Data are shown as mean ± SEM. Significance was assessed using one-way ANOVA test followed by Bonferroni-corrected post hoc test. The listed P values correspond to
1220   comparisons CON L5/6 vs. GE L5/6 and CON L2/3 vs. GE L2/3.
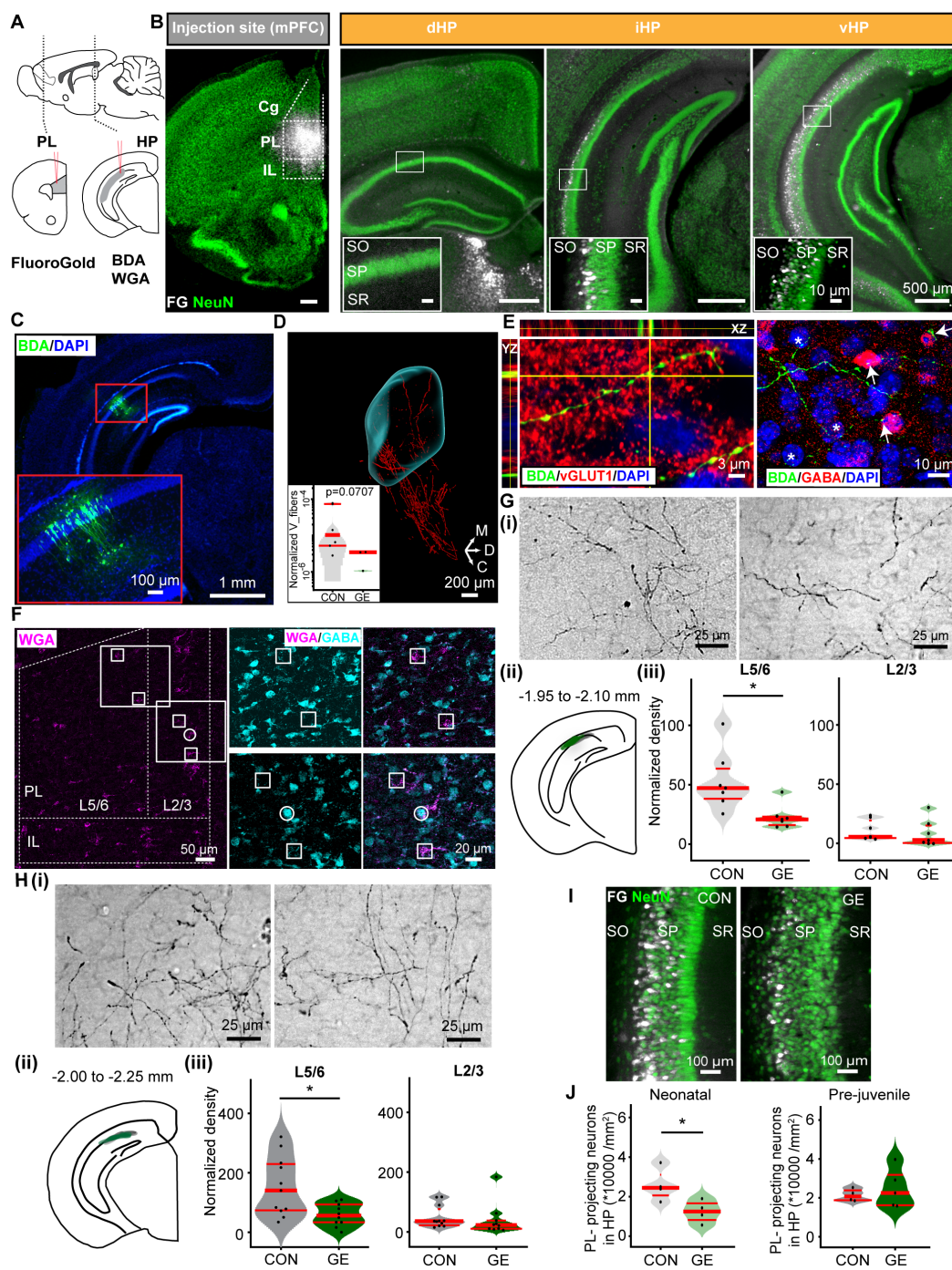1221

Figure 1 - Song et al.
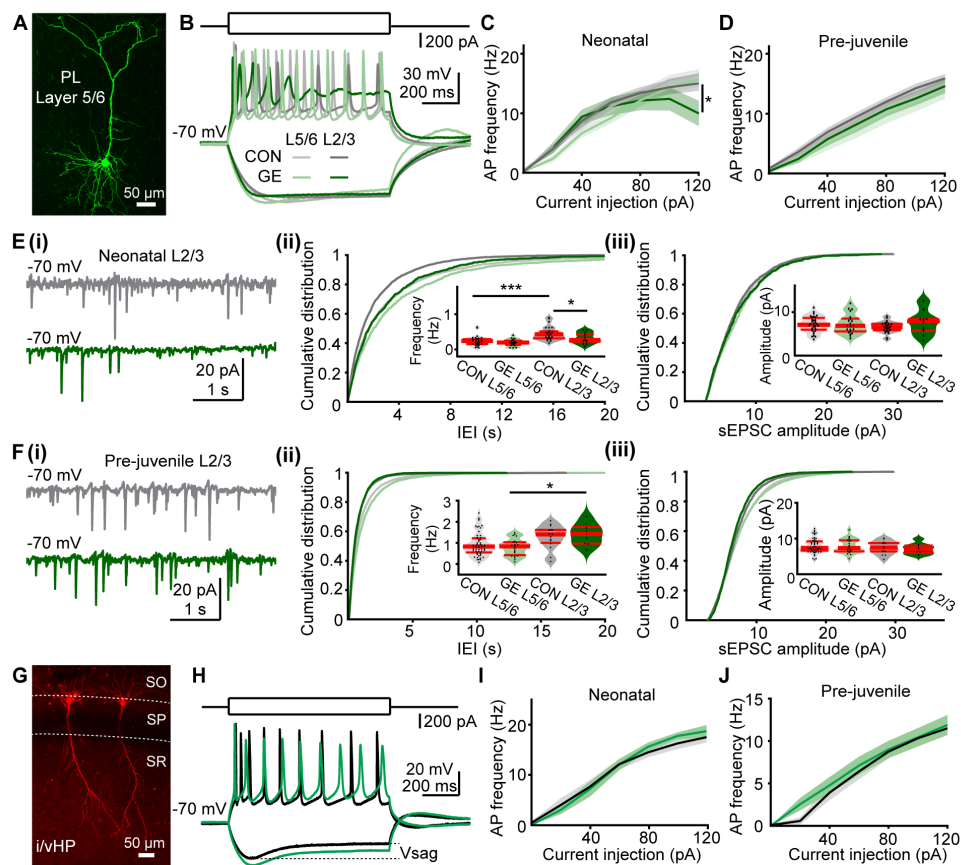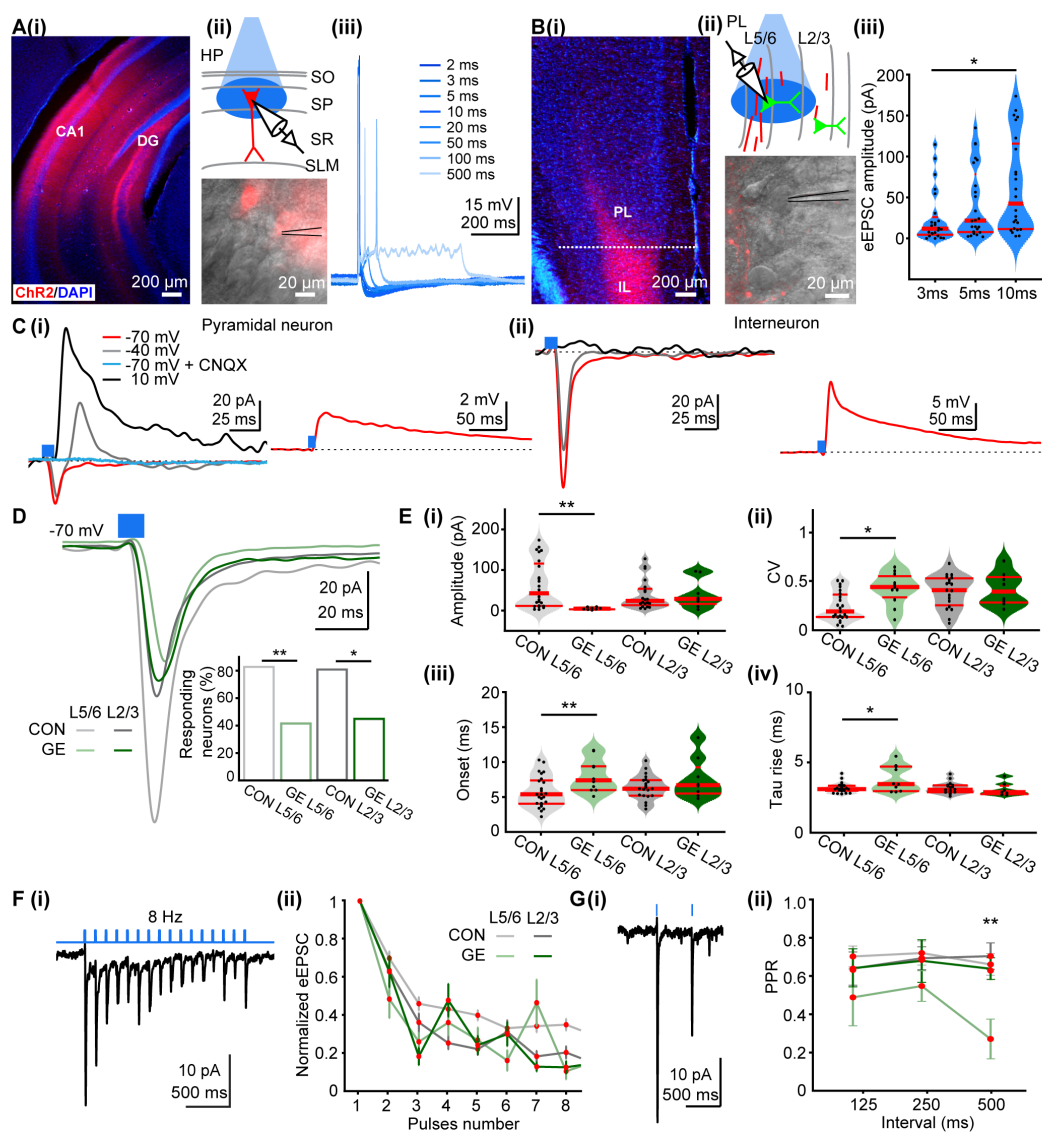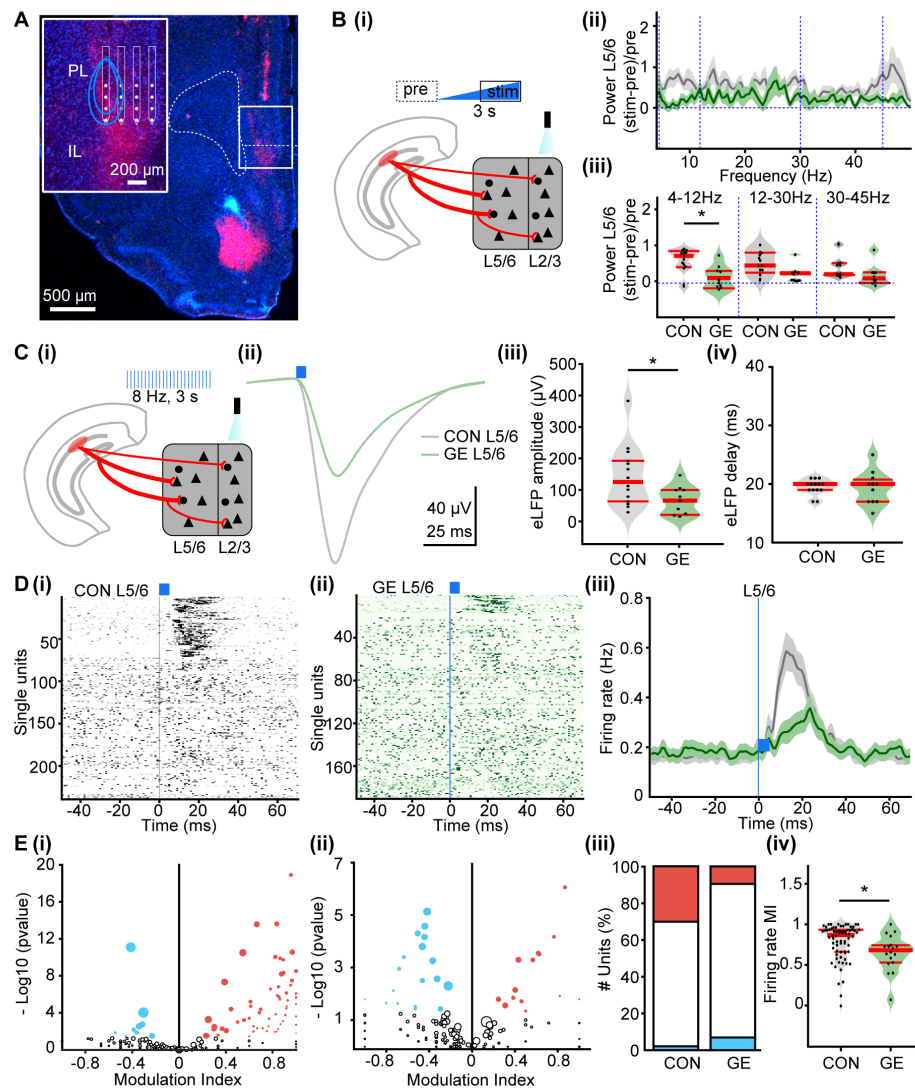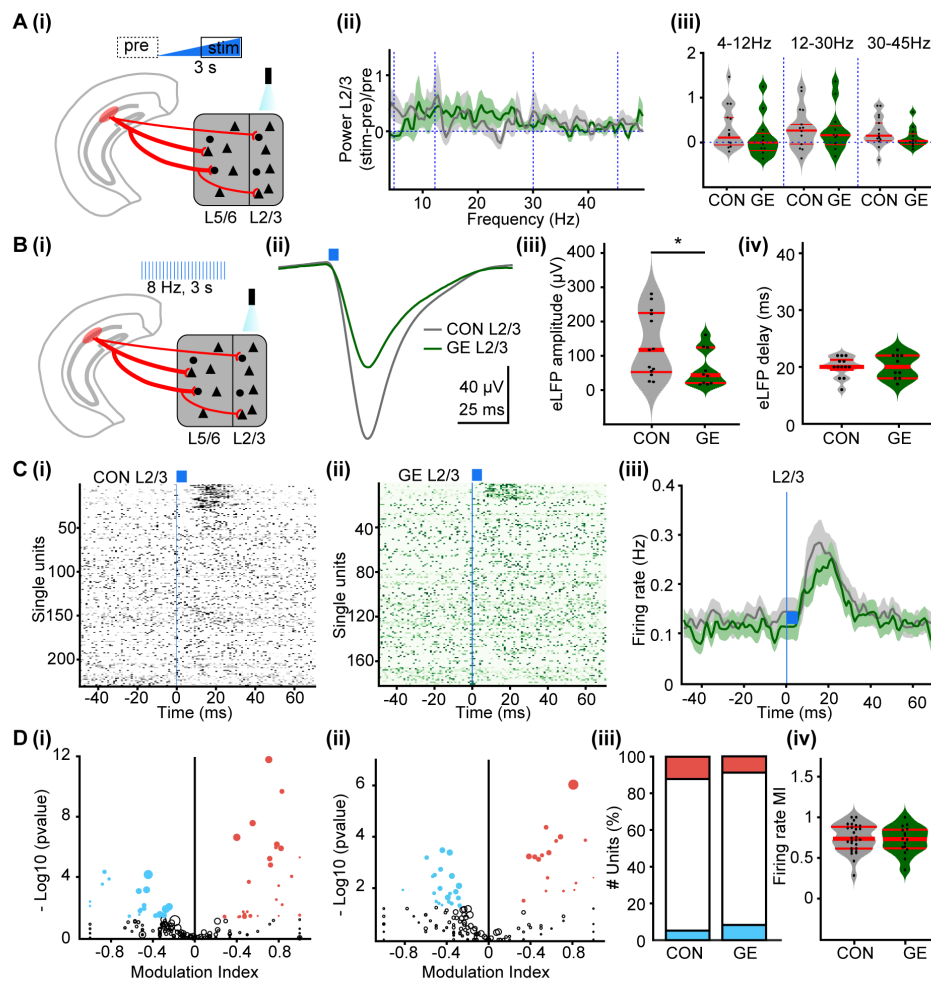
Figure 2 - Song et al.

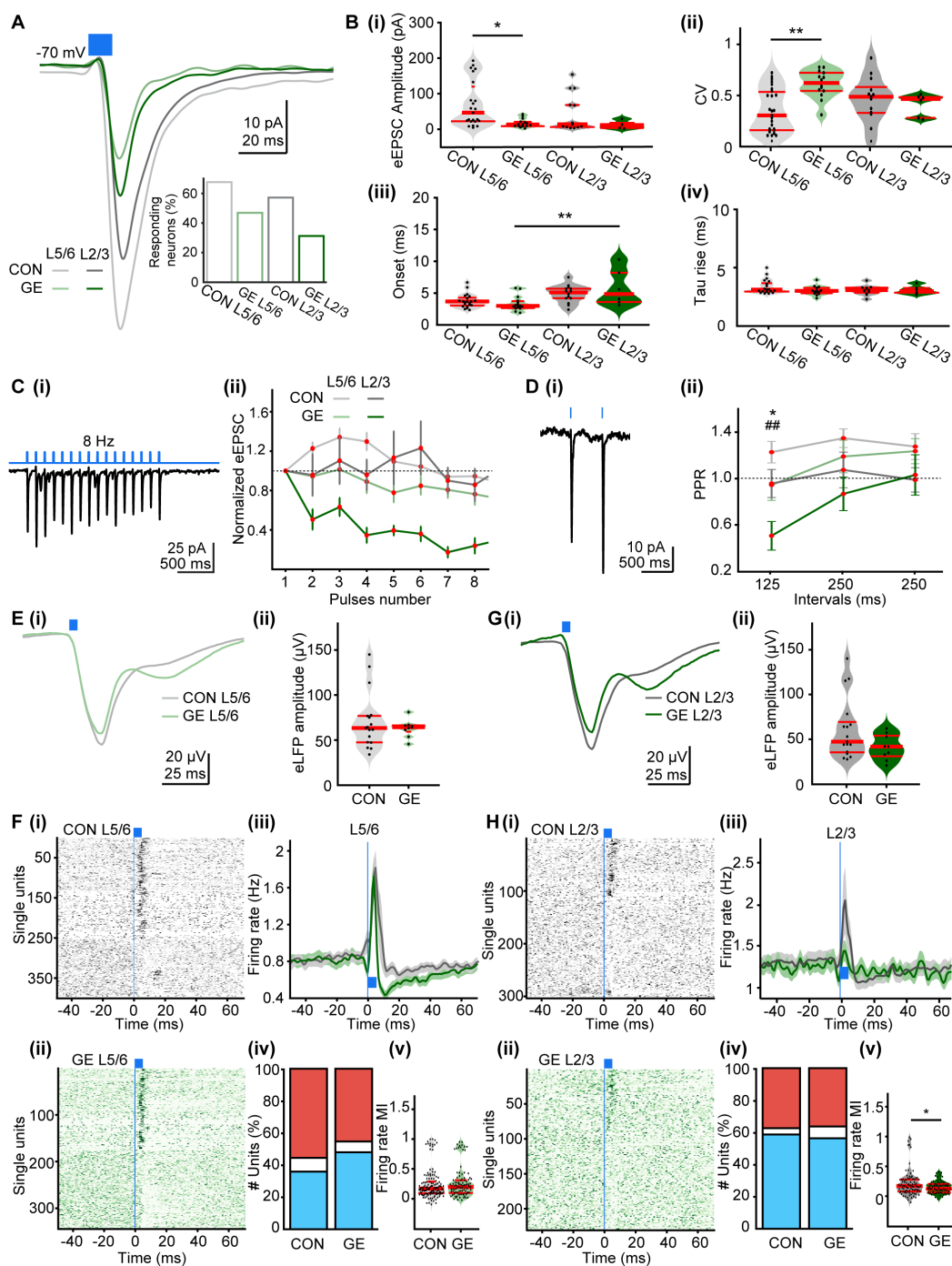Figure 3 - Song et al.

Figure 4 -Song et al.

Figure 5 - Song et al.

Figure 6 - Song et al.